Master Thesis
TVVR 25/5017

Numerical Modeling of Blue Carbon Dynamics Considering Seagrass at Sashiki Port

Taichi Tsuchiya

Division of Water Resources Engineering
Department of Building and Environmental Technology
Lund University

Numerical Modeling of Blue Carbon Dynamics Considering Seagrass at Sashiki Port

By:
Taichi Tsuchiya

Master Thesis

Division of Water Resources Engineering
Department of Building & Environmental Technology
Lund University
Box 118
221 00 Lund, Sweden

Water Resources Engineering
TVVR-25/5017
ISSN 1101-9824

Lund 2026
www.tvrl.lth.se

Master Thesis
Division of Water Resources Engineering
Department of Building & Environmental Technology
Lund University

English title:	Numerical Modeling of Blue Carbon Dynamics Considering Seagrass at Sashiki Port
Author(s):	Taichi Tsuchiya
Supervisor:	Shinichiro Yano Magnus Larson
Examiner:	Ronny Berndtsson
Language	English
Year:	2026
Keywords:	Climate change; Blue carbon; Carbon dioxide; Seagrass; Numerical model

Acknowledgements

I would like to express my sincere gratitude to my supervisor, Professor Shinichiro Yano in Kysuhu University, for his invaluable guidance and continuous support throughout the four years since I joined his laboratory, including my period of study in Lund. His insightful advice greatly shaped the direction of this research, and his encouragement during challenging moments—especially before the Master's thesis abstract deadline—was deeply appreciated.

I am also sincerely grateful to Professor Magnus Larson at Lund University for his guidance and for teaching the courses I attended during my study abroad program. The academic knowledge and international perspective I gained through his instruction significantly contributed to my development as a researcher. I also thank Professor Ronny Berndtsson for his careful review and support during the thesis writing process.

I am sincerely grateful to Associate Professor Yasuyuki Maruya for his technical advice and generous support, particularly in equipment troubleshooting and model development. When I encountered difficulties with the water quality experiments, he provided valuable guidance and kindly communicated with the equipment manufacturer on my behalf.

I would also like to express my gratitude to the professors and classmates in the Water Resources Engineering program at Lund University. Studying abroad was my first experience living outside Japan, and I was initially anxious about my English skills. However, their kindness and advice helped me greatly. Through discussions with them, I was able to deepen my academic knowledge and broaden my perspective.

I would like to express my heartfelt appreciation to my close friends, Ai Sanada and Shuhei Arita, who studied in Lund with me from Kyushu University. I would not have been able to complete my studies in Lund or finish this thesis without their support.

Finally, I would like to thank my family and friends for their constant encouragement and support throughout my time at Kyushu University and Lund University.

Abstract

Blue carbon, defined as carbon fixed by marine plants, has gained attention as a climate change mitigation strategy. Coastal ecosystems play an important role in blue carbon storage due to their high carbon burial rates. Although the dynamics of the partial pressure of CO_2 in seawater (pCO_2) are closely related to blue carbon processes, studies investigating pCO_2 variability in coastal areas remain limited. This study analyzes pCO_2 dynamics in a seagrass bed together with relevant environmental factors and seeks to improve an existing numerical model by incorporating seagrass biological processes. The study site is located on the eastern coast of the Yatsushiro Sea in Kumamoto Prefecture, Japan, with field observations conducted at Sashiki Port. A five-year dataset from six field surveys between 2021 and 2025 was used to evaluate the effects of varying environmental conditions on carbon dynamics. Model development was carried out using Delft3D, a hydrodynamic and water quality modeling framework. The results reveal the temporal variability of pCO_2 and identify its major controlling factors. Weather conditions strongly influenced air–sea CO_2 flux. Although incorporating seagrass processes improved model representation, simulated pCO_2 showed only moderate agreement with observations, highlighting the need for further parameter refinement and continued field measurements.

Table of contents

List of Figures

List of Tables

1. Introduction

1.1 Blue carbon

Climate change is one of the most serious global issues today. In Japan, natural disasters have become more intense due to global warming, causing greater damage to human life and property. One of the causes of climate change is the increase in greenhouse gases such as CO_2.

"Blue Carbon" has attention as an natural solution to mitigate climate change (Nellemann *et al*., 2009). Blue carbon refers to carbon fixed by marine plants through photosynthesis. In 2009, UNEP published the report, *Blue Carbon, A rapid response assessment*, which highlited the importance of marine ecosystems in carbon storage. The process of carbon fixation by marine organisms is shown in **Fig. 1.1**, and summarized as follows:

1. When the partial pressure of CO_2 in seawater (pCO_2) is less than that in the atmosphere, CO_2 is absorbed from the air to the sea.
2. Onece CO_2 is dissolved in seawater, CO_2 forms bicarbonate ion (HCO_3^-) and carbonate ion (CO_3^{2-}). The total amount of these inorganic carbon species is called dissolved inorganic carbon (DIC).
3. Marine organisms like phytoplankton and seagrass take up DIC through photosynthesis.
4. When marine organisms die, part of the organic matter is buried in sediment and can be stored there. The stored organic matter is preserved in the sediments without being decomposed for decades to thousands of years (Chambers *et al.*, 2001)
5. When DIC decreases, pCO_2 also does. As a result, this process above is promoted.

The annual carbon storage of blue carbon ecosystems is comparable to that of terrestrial plants. It is estimated that blue carbon accounts for 55% of carbon fixed by all plants on the earth although the blue carbon ecosystems cover only less than 0.5% of the seabed and represent only 0.05% of total terrestrial biomass (Nellemann *et al*., 2009). Especially, coastal areas, *i.e.* seagrass beds, mangroves, and salt marshes, are important in perspective of carbon burial, and these three areas have large carbon sink capacity. shows the area of each ecosystem and its organic carbon burial rate. As seen in **Table 1.1**, the area of vegetated habitats is 1.7 Million km^2 and is considerably less than that of other ecosystems. The organic carbon burial of vegetated areas accounts for 71 % of that of the ocean at maximum. In addition to that, as the evidence that the carbon sink capacity of the coastal areas is larger than that of the land, **Fig. 1.2** shows carbon burial rate of three kinds of forest (Green Carbon in this case) and blue carbon ecosystems. It is clear that the organic carbon burial of blue carbon ecosystem is greater than that of other ecosystems, and the sequestration rate of blue carbon ecosystem is greater than that of forest. This suggests that blue carbon ecosystems are highly efficient carbon sinks per unit area.

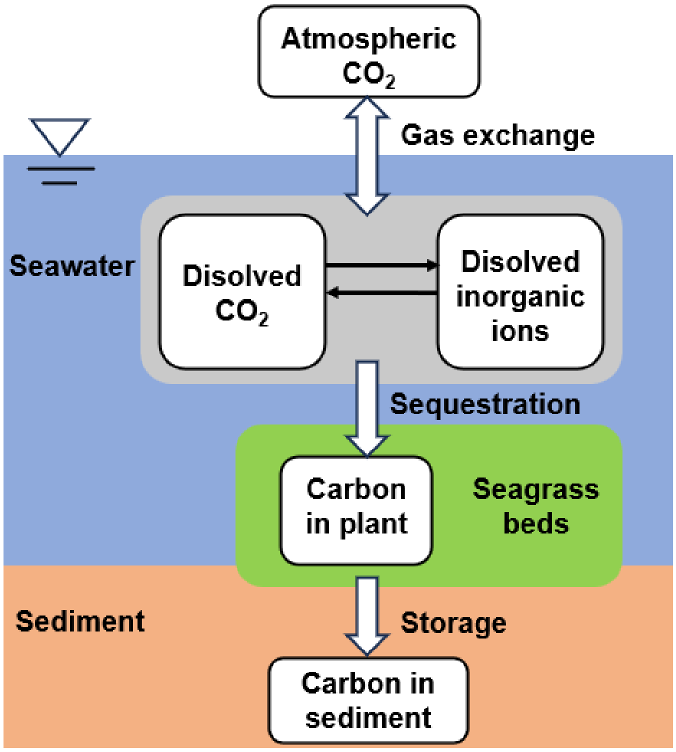

Fig. 1.1 Conceptual diagram of carbon fixation by marine organisms

Table 1.1 Mean and maximum (bracket) of coverage area of blue carbon sinks and carbon burial rates (Nellemann *et al*., 2009)

Component	Area	Organic Carbon Burial	
	Million km^2	Ton C ha^{-1} y^{-1}	Tg C y^{-1}
Vegetated habitats			
Mangroves	0.17 (0.3)	1.39, 0.20 – 6.54 (1.89)	17 – 23.6 (57)
Salt Marsh	0.4 (0.8)	1.51, 0.18 – 17.3 (2.37)	60.4 – 70(190)
Seagrass	0.33 (0.6)	0.83, 0.56 – 1.82 (1.37)	27.4 – 44 (82)
Total vegetated habitats	0.9 (1.7)	1.23, 0.18 – 17.3 (1.93)	114 – 131 (329)
Depositional areas			
Estuaries	1.8	0.5	81.0
Shelf	26.6	0.2	45.2
Total depositional areas			126.2
Total coastal burial			237.6 (454)
% Vegetated habitats			46.89 (0.72)
Deep sea burial	330.0	0.00018	6.0
Total oceanic burial			243.62 (460)
% Vegetated habitats			45.73 (0.71)

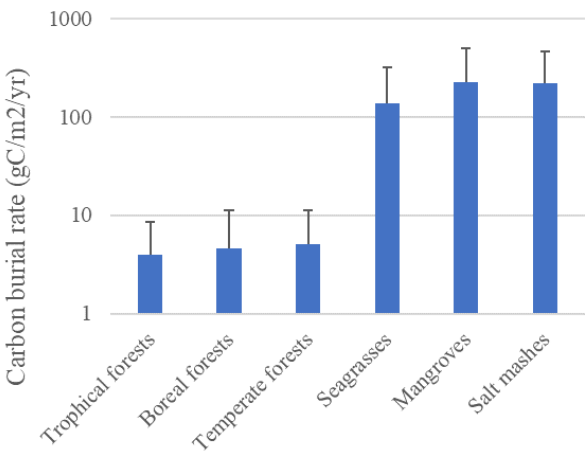

Fig. 1.2 Carbon burial rate of terrestrial and marine ecosystems (Mcleod *et al.,* 2011)

1.2 Carbon sink in seagrass beds

Seagrass is a flowering plant that grows in the sea, and is different from seaweed. In Japan, 16 species of seagrass have been reported (Ministry of the Environment, 2008). Among them, eelgrass (*Zostera marina*) is widely distributed in relatively calm coatal waters from Hokkaido to Kyushu (Ministry of the Environment, 2008) and grows abundantly at the study site. **Figure 1.3** is a picture of eelgrass beds in Nogita Port in Itoshima City in Japan. It is a different place from the study site.

Seagrass has roots, rhizomes, stems and leaves, and it can spread roots and rhizomes on the sandy and muddy seabed. Seagrass beds have high carbon burial rates for several reasons:

1. They are among the most productive ecosystems on the earth (Duarte *et al.*, 2010).
2. Dead plants and fallen leaves accumulate on the sandy and muddy seabed.
3. Seagrass reduces water flow, which promotes accumulation of organic matter.
4. Rhizomes stabilize seabeds and reduces resuspension of accumulated organic matter.
5. Sediments in seagrass beds are often anaerobic, slowing decomposition (Kristensen and Holmer, 2001; Moritsch *et al.*, 2025).

In contrast, seaweed is distinguished from seagrass because seaweed has no roots or rhizomes and is attached to rocks. Therefore, its carbon sink capacity is limited, compared to that of seagrass. However, seaweed is also one of ecosystems with the highest primary productivity, and it can still contribute to carbon sequestration when if transported to areas with high burial capacity, such as seagrass beds or to the deep sea (Arina *et al.*, 2023; Krause-Jensen and Duarte, 2016).


Fig. 1.3 Eelgrass bed in Nogita Port in Itoshima City in Japan

1.3 CO_2 sink in coastal areas

Although blue carbon ecosystems store carbon, the reduction of atmospheric CO_2 depends on air-sea gas exchange as shown in **Fig. 1.1**. Once seagrass captures carbon in seawater, DIC decreases, leading to the reduction of pCO_2. As a result, CO_2 is absorbed from the atmosphere into seawater through gas exchange. Therefore, it is necesarry to estimate not only carbon storage in biomass and sediments but also air-sea CO_2 flux in order to evaluate the role of seagrass beds as carbon sinks.

About one quarter of anthropogenic CO_2 emissions have been absorbed by the ocean over the past several decades (Gruber *et al.*, 2023). While the open ocean and continental shelf are generally considered CO_2 sinks in other research (*i.e.* Tsunogai *et al.*, 2002; Takahashi *et al.*, 2009), some coastal areas can act as CO_2 sources (Borges *et al.*, 2005). Borges *et al.* (2005) also emphasized that accounting for ecosystem diversity is essential when assessing whether the area functions as a net sink or a source of CO_2, as the estimates presented in their study involve considerable uncertainties. Similarly, it is important to consider the distribution of plants like seagrass when the CO_2 budget in coastal aras is estimated (Tokoro *et al.*, 2014). Coastal environments are highly complex compared to the relatively stable conditions of the open ocean. Environmental conditions in coastal areas can fluctuate over short time scales, ranging from several hours to days. Consequently, accurately estimating the amount of carbon absorbed in these regions is challenging.

pCO_2 is commonly used to quantify air-sea CO_2 exchange. As descrivbed in Section 1.1, when pCO_2 is lower than atmospheric pCO_2, CO_2 is absorbed from the atmosphere into the sea. Atmospheric pCO_2 remains relatively constant throughout the year. In contrast, pCO_2 in coastal areas varies greatly over time and space, driven by various factors including physical processes (e.g., currents and stratification), biological processes (e.g., photosynthesis and respiration), topography, and meteorological conditions. Furthermore, studies investgating pCO_2 in coastal areas remain limited (Macreadie *et al*., 2019).

Given this background, accumulating pCO_2 data under various conditions is essential to improve the accuracy of CO_2 uptake estimates in coastal areas (Macreadie *et al*., 2019).

1.4 Previous research in coastal areas

Previous observation studies have identified factors affecting pCO_2 in coastal areas. For examples, DIC, TA, and wind speed influence CO_2 flux in Furen Lake in Hokkaido (Tada *et al*., 2013) and Hashirimizu Coast in Kanagawa Prefecture (Tada *et al*., 2014). Especially, wind speed directly affects air-sea CO_2 gas exchange while biological processes influence CO_2 indirectly through changes in DIC (Tada *et al*., 2013).

Numerical modeling studies have also been conducted. Tada *et al*. (2018) developed a model to simulate pCO_2 dynamics based on observation data of Tada *et al*. (2013). Kuwae *et al*. (2018) applied an ecosystem model to Tokyo Bay and analyzed air-sea CO_2 flux dynamics and the factors.

However, studies combining detailed observation and numerical modeling remain limited. Especially, studies focusing on Kyushu region like the Yatsushiro Sea and the Ariake Sea are fewer than other regions.

1.5 Previous research in the Yatsushiro Sea

Several studies have been conducted in the Yatsushiro Sea since 2018. Saito *et al*. (2020) investigated pCO_2 dynamics under three different mixing conditions (*i.e.*, strong stratified, weak stratified, and mixed condition) in 20218 and 2019. The study site was near the mouth of the Kuma River, where submerged macrophytes like seagrass do not exist.. They found that pCO_2 decreases during strong stratification due to phytoplankton photosynthesis,.and air-sea

CO_2 flux during daytime from 6 am to 6 pm was generally negative It means that CO_2 was absorbed from the air to the sea regardless of the mixing condition. (Saito *et al.*, 2020).

Komori *et al*. (2021) developed a model to simulate pCO_2 dynamics related to freshwater inflow from the Kuma River to the Yatsushiro Sea based on the results of previous observation. Xiong *et al*. (2022) also developed a model to simulate pCO_2 dynamic, taking stratification into account. Their study revealed that pCO_2 fluctuates significantly in space and time. For example, pCO_2 was released into the atmosphere immediately after freshwater inflow; however, it was subsequently absorbed as phytoplankton blooms promote photosynthesis in the mixed seawater. While those models showed good reproducibility—for instance, the model of Komori *et al.* (2021) with correlation coefficients for DIC, total alkalinity (TA), and pCO_2 of 0.940, 0.937, and 0.841, and RMSPE for DIC, TA, and pCO_2 of 1.90 %, 2.02 %, and 14.48 %, respectively—further improvements are needed. Specifically, incorporating the biological processes of seagrass is essential for a more accurate simulation of pCO_2 (Komori *et al*., 2021; Xiong *et al*., 2022).

1.6 Aim

As described before, it is important to collect observation data of pCO_2 and related factors under various environmental conditions and make a model simulating pCO_2 based on the observation results for clarifying pCO_2 dynamics in coastal areas. Even in the eelgrass beds on the eastern coast of the Yatsushiro Sea (Nosaka-no-ura, Ashikita Town), the subject area of this study, the impact of complex flow and water quality fluctuation characteristics on pCO_2 dynamics has not been fully understood. Therefore, aims of this study are followings:

- To analyze the effects of physical factors (e.g., solar radiation and tides) and biological processes (e.g., photosynthesis and respiration, represented by ΔDIC) on pCO_2, based on five years of field observations (2021-2025).
- To identify the main controlling factors of carbon dynamics using multiple regression analysis.
- To quantify air-sea CO_2 flux in the study area.
- To improve the existing pCO_2 model by incorporating seagrass (eelgrass) processes.

2. Methodology

2.1 Study area

The study area is the Yatsushiro Sea, located on the west coast of Kyushu, Japan (see **Fig. 2.1**). It is surrounded by Kumamoto Prefecture, Kagoshima Prefecture and the Amakusa Islands. The sea connects to the East China through narrow straits such as the Nagashima and Hayasaki Straits. Becuase of these narrow openings, water exchnage with the open ocean is limited. Therefoere, the Yatsushiro Sea is a representative semi-enclosed coastal sea.

It possesses the second-largest tidal range in Japan, reaching about 4 m at Yatsushiro Port. It is surpassed only by the neighboring Ariake Sea. These unique features have fostered a highly productive environment, most notably supporting a flourishing aquaculture industry. Consequently, the region maintains a distinct ecosystem characterized by high biological productivity and significant socio-economic importance.

The southern Yatsushiro Sea and the waters around the Amakusa Islands are important in perspective of biodiversity. The Tsushima Warm Current flow into coast in Kumamoto Prefecture, and large range of reef-building coral is distributed mainly around the Amakusa Islands. Although this is a temperate zone, both eelgrass and coral habitats exist. According to surveys of Ministry of the Environment (2021), seagrass beds cover about 2,385 ha in the southern Ariake Sea and the Yatsushiro Sea.

The area of the Yatsushiro Sea is approximately 1,200 km^2. Several rivers flow into the Yatsushiro Sea and their drainage area is about 3,000 km^2. The largest is the Kuma River, with a drainage area of 1,880 km^2. River discharge strongly affects salinity, nutrients, and carbon dyanamics in the coastal area.

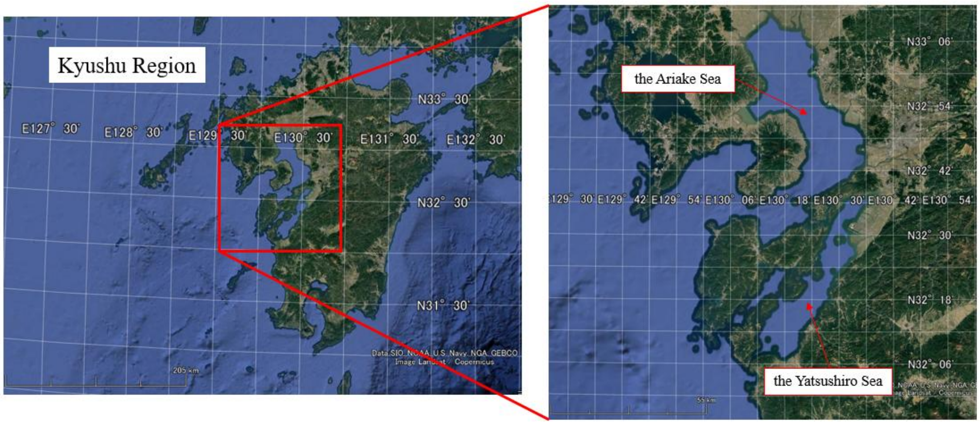

Fig. 2.1 Study area (Created by Google Earth Pro)

2.2 Field Observation

Field observations were conducted at an eelgrass bed in Sashiki Port, located in Ashikita Town on the eastern coast of the Yatsushiro Sea. **Figure 2.2** and **Figure 2.3** shows the location of observation points. The study site is the inlet called Nosaka-no-ura, where the Sashiki River and the Yunoura River flow into. The port is protected by a breakwater approximately 850 m long and it prevents waves and sediments from coming in. Eelgrass grows along the inner side of the breakwater (blue ellipse in **Fig. 2.3**). **Figure 2.4** is a photograph of eelgrass at observation points.

Observations were carried out once or twice a year from 2021 to 2025. **Table 2.1** presents the detail information of observation. Surface water samples were collected at each observation point every few hours, roughly at high and low tides, using buckets (see **Fig. 2.5**) Water temperature and salinity were measured on site using a multi-parameter water quality meter (ProDSS, YSI Inc.) as seen in **Fig. 2.6**.

Water samples were collected at three points (St. A, B, and C) from 2021 to 2023. In 2024 and 2025, sampling was conducted only St. B. Water samples were stored in 250 mL Duran bottles, and immediately afterwards, mercuric chloride was injected to stop the biological activity and preserve DIC. Later, DIC and TA were measured using laboratory instruments; a flow-through carbonate system separator (MDO-02, Kimoto Electric Co., Ltd.) and a total alkalinity titrator (ATT-15, Kimoto Electric Co., Ltd.). pCO_2 was calculated from water temperature, salinity, DIC, and TA using carbonate system equilibrium equations.

Fig. 2.2 Location of the field observation (Created by Google Earth Pro)

Fig. 2.3 Location of observation points (Red and Yellow circle) and eelgrass bed (Blue ellipse) (Created by Google Earth Pro)

Fig. 2.4 Photograph of the seagrass bed at the observation points (May 2025)

Table 2.1 Detailed information of observation

Date	Frequency	Observation point	Weather	Tide (St. Minamata)
26-27 Jun 2021	8 times in total (3 hours interval)	3 points	Light rain	Spring tides
10-11 Jun 2022	9 times in total (3 hours interval)		Light rain	
16-17 May 2023	10 times in total (3 hours interval)		Sunny	
7-8 Jun 2024	7 times in total (3 hours interval)	1 point	Cloudy	
13-14 May 2025			Sunny	
19-20 May 2025			Sunny	Neap tides

Fig. 2.5 Photograph of sampling water at seagrass bed (May, 2025)

Fig. 2.6 Photograph of measuring water temperature and salinity (May, 2025)

2.3 Calculation of pCO_2

pCO_2 was calculated from water temperature, salinity, DIC, and TA using chemical equilibrium equations of the carbonate system in shown Eq. (2.1) to Eq. (2.7).

The calculation follows the formulation presented by Zeebe(2001). The equations describe the balance among dissolved CO_2, bicarbonate, and carbonate ions under equilibrium conditions.

$$\begin{aligned}\mathrm{DIC}\cdot(K_B^*+h)\cdot(K_1^*h^2+2K_1^*K_2^*h)\\ =[\mathrm{TA}(K_B^*+h)h-K_B^*B_Th-K_W^*(K_B^*+h)\\ +(K_B^*+h)h^2]\cdot(h^2+K_1^*h+K_1^*K_2^*\end{aligned} \quad \text{Eq. (2.1)}$$

$$\begin{aligned}\ln K_1^* = 2.83655-\frac{2307.1266}{T}-1.5529413\ln T\\ -\left(0.207608410+\frac{4.0484}{T}\right)\sqrt{S}+0.0846834S\\ -0.00654208S^{3/2}+\ln(1-0.001005S)\end{aligned} \quad \text{Eq. (2.2)}$$

$$\begin{aligned}\ln K_2^* = -9.226508-\frac{3351.6106}{T}-0.2005743\\ -\left(0.106901773+\frac{23.9722}{T}\right)\sqrt{S}\\ +0.1130822S-0.00846934S^{3/2}\\ +\ln(1-0.001005S)\end{aligned} \quad \text{Eq. (2.3)}$$

$$\begin{aligned}&\ln K_B^*\\ &=\frac{-8966.90-2890.53S^{1/2}-77.942S+1.728S^{3/2}-0.0996}{T}\\ &+148.0248+137.1942S^{1/2}+1.62142S-(24.4344\\ &+25.085S^{1/2}+0.2474S)\ln T+0.053105S^{1/2}\,T\end{aligned} \quad \text{Eq. (2.4)}$$

$$B_T = 4.16\cdot10^{-4}\frac{S}{35} \quad \text{Eq. (2.5)}$$

$$\begin{aligned}\ln K_W^* = 148.96502-\frac{13847.26}{T}-23.6521\ln T\\ +\left[\frac{118.67}{T}-5.977+1.0495\ln T\right]S^{1/2}\\ -0.01615S\end{aligned} \quad \text{Eq. (2.6)}$$

$$s = DIC/(1+\frac{K_1^*}{h}+\frac{K_1^*K_2^*}{h^2}) \quad \text{Eq. (2.7)}$$

Where K_1^* and K_2^* are acidity constant, K_B^* is the dissociation constant of boric acid, B_T is the total borate concentration, K_W^* is the ion product of water, h is the hydrogen ion concentration, T is the absolute temperature (K), S is the salinity, and s is the partial pressure of CO_2 in water (µatm).

2.4 Air-sea CO_2 Flux

The air-sea CO_2 flux F can be calculated using the bulk formula (Eq. (2.8)), which uses the CO_2 partial pressure difference between the atmosphere and seawater. A positive value indicates "emission" from seawater to the atmosphere, and a negative value indicates "absorption" from the atmosphere to seawater.

$$F = k \cdot S \cdot (pCO_{2\,water} - pCO_{2\,air}) \qquad \text{Eq. (2.8)}$$

Where F is the air-sea CO_2 flux (μmol/m^2/s), k is the gas transfer velocity (m/s), S is the CO_2 solubility in seawater (mol/(m^3·atm)), and $pCO_{2\,water}$ and $pCO_{2\,air}$ are the partial pressure of CO_2 in seawater and air (μatm), respectively.

The CO_2 solubility coefficient K_0 (mol/(l·atm)) in seawater can be calculated using the empirical formula of Weiss (1974) as shown in Eq. (2.9) and Eq. (2.10). The gas transfer velocity k was calculated using Eq. (2.11) proposed by Wanninkhof (1992), which depends on wind speed and the Schmidt number as shown in Eq.(2.12) to Eq. (2.14).

$$lnK_0 = -58.0931 + 90.5069 * \left(\frac{100}{T}\right) + 22.2940 * ln\left(\frac{T}{100}\right) + S * [0.027766 + (-0.025888) * \left(\frac{T}{100}\right) + 0.0050578 * \left(\frac{T}{100}\right)^2] \qquad \text{Eq. (2.9)}$$

$$T = t + 273.15 \qquad \text{Eq. (2.10)}$$

Where S is absolute salinity (‰), and T and t are water temperature (K) and (^oC), respectively.

$$k = 0.39 * U_{10}^2 * \left(\frac{S_c}{660}\right)^{-0.5} \qquad \text{Eq. (2.11)}$$

Where U_{10} is the wind speed (m/s) at a height of 10 m above the water surface, and Sc is a parameter called the Schmidt number, which is known to vary linearly with salinity (Borges *et al.*, 2004). Sc can be calculated using the empirical formulas Eq. (2.12) to Eq. (2.14) (Wanninkhof, 1992).

$$S_c = \frac{S_{c,sea} - S_{c,fresh}}{35} * S + S_{c,fresh} \quad \text{Eq. (2.12)}$$

$$S_{c,sea} = (2073.1 - 125.62 * t + 3.6276 * t^2 - 0.043219 * t^3) \quad \text{Eq. (2.13)}$$

$$S_{c,fresh} = (1911.1 - 118.11 * t + 3.4527 * t^2 - 0.041320 * t^3) \quad \text{Eq. (2.14)}$$

Where $S_{c,sea}$ is the Schmidt number for open seawater (S = 35), $S_{c,fresh}$ is the Schmidt number for freshwater (S = 0), and t is the water temperature (°C).

Wind speed data were obtained from AMeDAS stations. The wind speed was corrected to 10 m height using a power-law profile as presented in Eq. (2.15), following Ishizaki and Mitsuta (1962). The wind speed was converted to over-ocean wind speed using Carruthers' conversion coefficients from geostrophic wind to sea-surface wind, as cited by Arakawa *et al*. (2007) (see **Table 2.2**). Assuming that the AMeDAS station is located on land with significant surface roughness due to surrounding obstacles, the ratio of observed surface wind speed to geostrophic wind speed is 0.3. Since the ratio of sea-surface wind speed to geostrophic wind speed is 0.6, the ratio of sea-surface wind speed to observed surface wind speed is calculated as 0.6 / 0.3 = 2. Therefore, the observed wind speed was multiplied by a factor of two to obtain the corresponding sea-surface wind speed.

Atmospheric pCO_2 was determined using CO_2 concentration data from Ryori monitoring station of the Japan Meteorological Agency. It is known that atmospheric CO_2 concentration numerically approximates atmospheric pCO_2 (Nishimura *et al*., 1998).

$$U_{10} = U_Z \cdot \left(\frac{10}{Z}\right)^{\frac{1}{n}} \quad \text{Eq. (2.15)}$$

Where U_{10} denotes the wind speed (m/s) at height Z (m) above the sea surface, and $1/n$ is the power-law exponent determined by the surface roughness conditions at the observation site. The exponent was determined based on the guidelines of the Japan Road Association (2007).

Table 2.2 Relationship between the observed wind speed (*V*) and the geostrophic wind speed (V_g) proposed by Carruthers (Arakawa *et al*., 2007)

Location	Ratio of wind speed (V/V_g)
Open sea	0.60
Low island	0.55
Windward coast (adjacent to low land)	0.50
Leeward coast (adjacent to low land or sea)	0.40
Open flat land with few obstacles	0.40
Built-up or urban area with many obstacles	0.30

2.5 DIC and TA

2.5.1 General description for DIC and TA

Dissolved inorganic carbon (DIC) is the total amount of dissolved CO_2, bicarbonate ion and carbonate ion in seawater as shown in Eq. (2.16). These components are in chemical equilibrium. For example, when dissolved CO_2 increases, the part of CO_2 changes to bicarbonate ion and carbonate ion to keep equilibrium condition. Generally, DIC decreases due to photosynthesis and increases due to respiration and decomposition of organic matter. DIC has positive correlation with pCO_2.

$$DIC = [CO_2] + [HCO_3^-] + [CO_3^{2-}] \qquad \text{Eq. (2.16)}$$

Total alkalinity (TA) is the total capacity of seawater to neutralize hydrogen ions. One of the most general equation is shown in Eq. (2.17) (Dickson, 1981). When TA is low, bicarbonate and carbonate ions are converted into dissolved CO_2 to neutralize the charge in the water, leading to rise of pCO_2. TA decreases due to calcification by corals and other organisms and increases during dissolution. TA and pCO_2 are negatively correlated. In fact, coral reefs are known to be a source of CO_2 because they have low TA and high pCO_2 (Ware *et al*., 1992).

$$\begin{aligned} TA = {} & [HCO_3^-] + 2[CO_3^{2-}] + [B(OH_4)^-] + [OH^-] \\ & + [SiO(OH)_3^-] + [HPO_4^{2-}] + 2[PO_4^{3-}] \\ & + [NH_3] + [HS^-] - [H^+] \end{aligned} \qquad \text{Eq. (2.17)}$$

2.5.2 Calculation of ΔDIC and ΔTA

To evaluate biological effects, ΔDIC and ΔTA were calculated. When there is no influence of biological processes, DIC and TA can be calculated from the simple mixing ratio of freshwater and open seawater by assuming that the endmembers at the inflow/outflow boundary are in a steady state. **Fig. 2.7** shows a conceptual diagram for calculating ΔDIC. ΔTA can also be calculated in a similar manner.

First, endmember values of DIC and TA for river water and offshore seawater were defined. In this study, river water endmembers were determined using samples collected at the Sashiki River and the Yunoura River as shown in **Fig. 2.8** and **Fig. 2.9**, respectively. The offshore seawater endmember was defined using KSSW (Kuroshio Subsurface Water) samples reported in a previous study (Qu *et al.*, 2018).

For a given salinity, DIC and TA were compared with the theoretical mixing line between freshwater and seawater. The deviation from this line was defined as ΔDIC or ΔTA. These values represent biological changes.

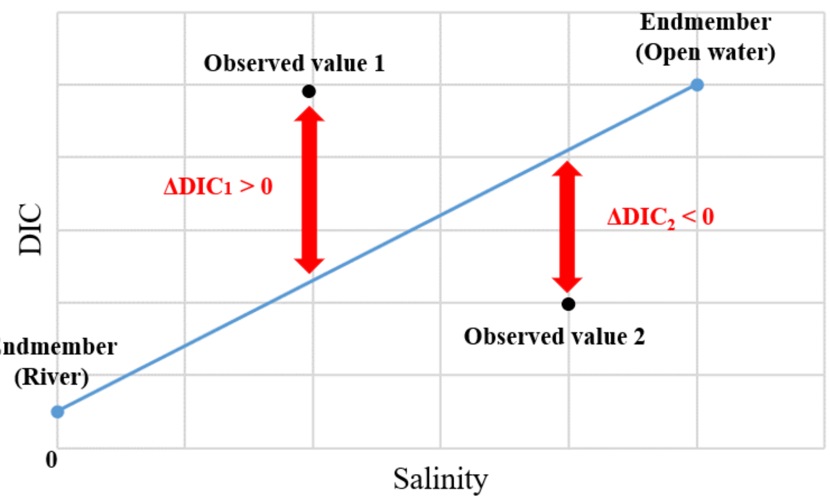

Fig. 2.7 Schematic diagram of the calculation of ΔDIC (ΔTA was calculated in the same manner)

Fig. 2.8 Observation point of the Sashiki River (32° 17’ 41” N, 130°30' 59" E) (May, 2025)

Fig. 2.9 Observation point of the Yunoura River (32° 16’ 29”, 130° 30’ 03” E) (May, 2025)

2.6 General description of numerical model

This study utilized Delft3D developed by Deltares, which is a comprehensive modeling framework capable of simulating various coastal and riverine processes, including flow, substance transport, and waves. Specifically, Delft3D-FLOW (3D flow simulation) and Delft3D-WAQ (water quality) modules are employed. **Figure 2.10** shows the study flow.

First, the Flow Model was developed in Delft3D-FLOW. The model calculated water temperature, salinity, flow velocity, *etc.* These results were used as input data to calculate DIC and TA in Low Trophic Level Ecosystem Model (LTLE Model). Delft3D-WAQ was used to improve the existing LTLE Model.

Finally, pCO_2 was calculated from water temperature, salinity, DIC, and TA using carbonate equilibrium equations because pCO_2 cannot be calculated directly in the model. By referring to previous research (Tadokoro and Yano, 2019; Komori *et al*, 2021. *etc*.), the model parameters were adjusted to reproduce observation data from 2022 and 2023 since these years were selected to represent contrasting weather conditions: cloudy and rainy in 2022, and clear and sunny in 2023.

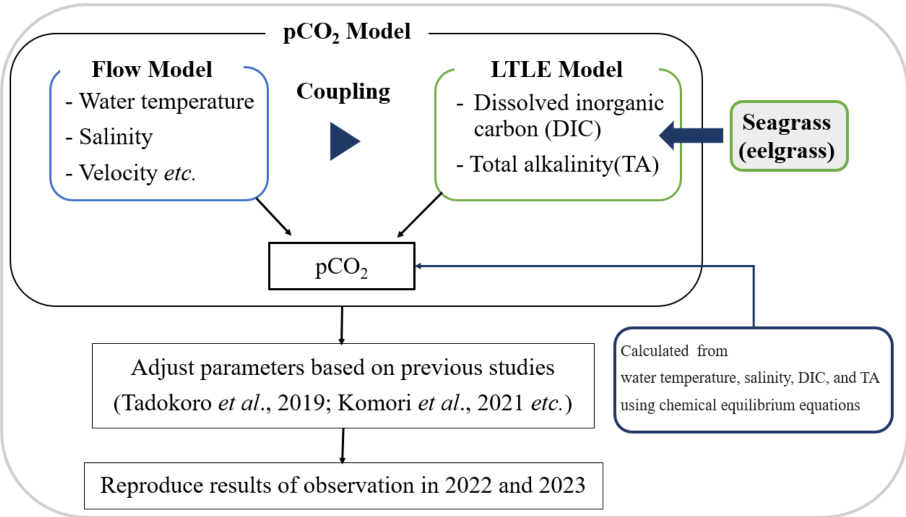

Fig. 2.10 Flow of model improvement

2.7 Flow Model

Delft3D-FLOW was used for flow simulation in this study. Delft3D-FLOW is a multi-dimensional hydrodynamic and transport simulation program The simulation domain included both the Ariake Sea and the Yatsushiro Sea, which are connected to each other (see **Fig. 2.11**). The study area is the Yatsushiro Sea, but it is important to include the Ariake Sea in the area for reproducing observation results accurately (Tanaka *et al*., 2002). The model used a horizontal resolution of approximately 250 m in a Cartesian coordinate system and a vertical resolution of 17 layers in a σ-coordinate system. These 17 layers were distributed with specific thicknesses to better capture vertical gradients as shown in **Fig. 2.12**, assigned as follows: 2% for each of the top 10 layers, 5% for the 11th layer, 10% for the next 3 layers, and 15% for the bottom 3 layers. The calculation spin-up period was 2 months with a time step of 2 min.

The open boundary conditions were set on a line connecting Kabashima Channel in (Nagasaki Pref.) and Akune (Kagoshima Pref.), with 40 tidal components as same as Komori *et al*. (2021).

Freshwater inflow was accounted for using hourly discharge from eight Class A rivers (the Chikugo River, the Yabe River, the Kase River, the Rokkaku River, the Kikuchi River, the Shirakawa River, the Midori River, and the Kuma River) and nine Class B rivers (the Kajima River, the Shiota River, the Seki River, the Tsuboi River, Hi River, the Otsubo River, the Sashiki River, the Yunoura River, and Minamata River). The Honmyo River is also shown in **Fig. 2.11,** but it was not considered in the model because it connects to the regulating reservoir in the Isahaya Bay and it does not affect the Ariake Sea. The hourly flow rates of Class A rivers were gained from Ministry of Land, Infrastructure, Transport and Tourism Hydrological Water Quality Database. The discharge for each river were calculated based on data at the nearest observation station to its river mouth. The lacked data were interpolated using values before and after that lacked value. Moreover, to take into account the discharge flowing downstream from the staitons, the discharge at the observatory was corrected by multiplying it by a coefficient calculated by dividing the total catchment area of the river by the catchment area of the observatory as shown in Eq. (2.18). For Class B rivers, the calculation was based on the catchment area ratio to nearby Class A rivers as shown in Eq. (2.19). These concepts are summarized in **Fig. 2.13**.

$$Q_A = Q_{obs} \times \frac{C_2}{C_1} \qquad \text{Eq. (2.18)}$$

$$Q_B = Q_{A.near} \times \frac{C_B}{C_{A,near}} \qquad \text{Eq. (2.19)}$$

Where Q_A is the discharge of Class A river (m^3/s), Q_{obs} is the discharge at observatory (m^3/s), C_1 is the upstream catchment area of observatory (km^2), C_2 is the total catchment area (km^2), Q_B is the discharge of Class B river (m^3/s), $Q_{A.near}$ is the discharge of a nearby Class A river (m^3/s), $C_{A,near}$ is the catchment area of a nearby Class A river (km^2), and C_B is the catchment area of Class B river (km^2).

Meteorological data, including solar radiation and wind, were obtained from St. Kumamoto and St. Minamata of the Japan Meteorological Agency's (AMeDAS), respectively. For seawater temperature at the open boundary, sea surface temperature and 50 m depth water temperature data were gained from the daily oceanographic information from the Fukuoka Regional Meteorological Observatory.

The horizontal eddy viscosity and eddy diffusion coefficients were evaluated using the SGS model, and the vertical eddy viscosity and eddy diffusion coefficients were evaluated using the *k*-*ε* model.

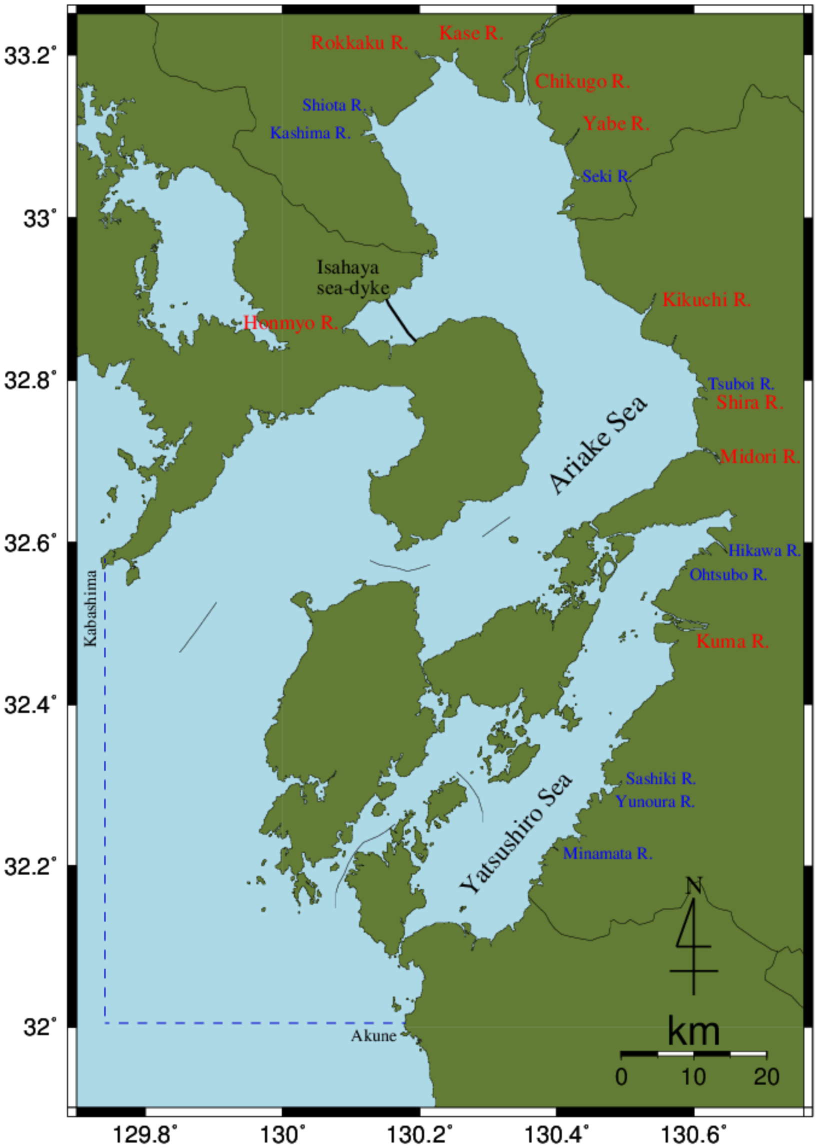

Fig. 2.11 Simulation domain (Class A rivers in red and Class B rivers in blue)

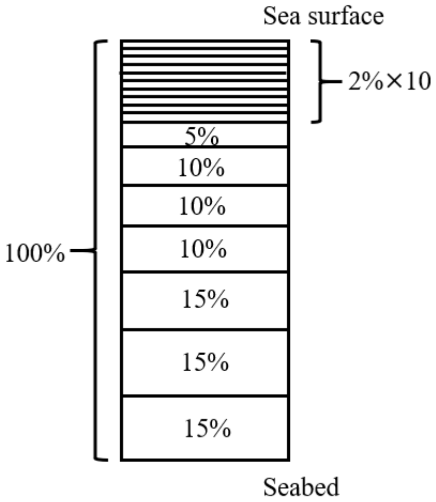

Fig. 2.12 Thickness of each layer

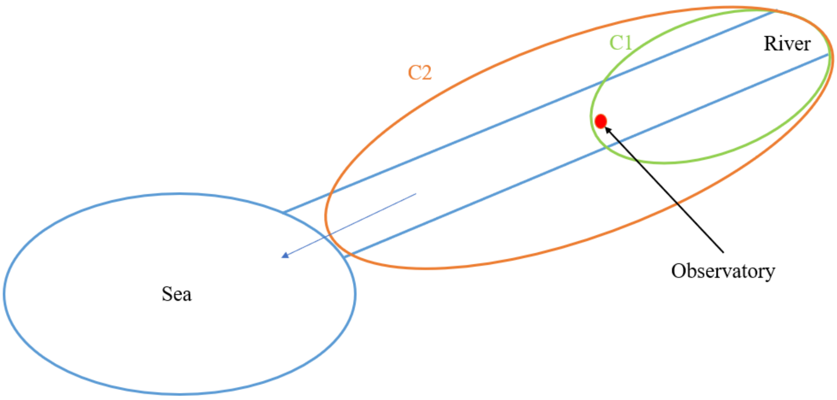

Fig. 2.13 Estimation of discharge

2.7.1 Background eddy value

In Delft3D-FLOW, background horizontal eddy viscosity and diffusivity can be set. Viscosity and diffusivity values calculated in sub grid model in Delft3D-FLOW were added to background eddy values, respectively. Both of them depend on grid size used in simulation. Generally speaking, they are 10 to 100 m^2/s when the grid size is coarse like hundreds of meters. In this study, the value of them is same as that of Komori *et al.* (2021). **Table 2.3** shows set values in this study. Specifically, the k-ε turbulence model was used to determine the vertical eddy viscosity.

Table 2.3 Background eddy value

	Set value	Default value	Recommended value in Delft3D manual
Horizontal eddy viscosity	80	10	10 to 100
Horizontal eddy diffusivity	10	10	10 to 100
Vertical eddy viscosity	1.0E-6	1.0E-6	1.0E-4 to 1.0E-3 in stratified waters
Vertical eddy diffusivity	1.0E-6	1.0E-6	-

2.7.2 Fundamental equation

The fundamental equations of flow are the three-dimensional equation of motion in a rotating Cartesian coordinate system, the continuity equation, the density equation, and the salt and heat transport equations shown in Eq. (2.20) to Eq. (2.26). They are explained briefly below, but for details, refer to the Delft3D manual (Deltares, 2018).

・Equation of motion (Reynolds-Averaged Navier-Stokes equation)

$$\frac{\partial U}{\partial t} + (\boldsymbol{v} \cdot \nabla) \cdot U - fV = -\frac{1}{\rho}\frac{\partial p}{\partial x} + \frac{1}{\rho}\left(\frac{\partial}{\partial x}\tau_{xx} + \frac{\partial}{\partial y}\tau_{yx} + \frac{\partial}{\partial z}\tau_{zx}\right) \quad \text{Eq. (2.20)}$$

$$\frac{\partial V}{\partial t} + (\boldsymbol{v} \cdot \nabla) \cdot V + fU = -\frac{1}{\rho}\frac{\partial p}{\partial y} + \frac{1}{\rho}\left(\frac{\partial}{\partial x}\tau_{xy} + \frac{\partial}{\partial y}\tau_{yy} + \frac{\partial}{\partial z}\tau_{zy}\right) \quad \text{Eq. (2.21)}$$

$$\frac{\partial W}{\partial t} + (\boldsymbol{v} \cdot \nabla) \cdot W = -g - \frac{1}{\rho}\frac{\partial p}{\partial z} + \frac{1}{\rho}\left(\frac{\partial}{\partial x}\tau_{xz} + \frac{\partial}{\partial y}\tau_{yz} + \frac{\partial}{\partial z}\tau_{zz}\right) \quad \text{Eq. (2.22)}$$

・Continuity equation

$$\frac{\partial \rho}{\partial t} + \nabla \cdot \rho \boldsymbol{v} = 0 \quad \text{Eq. (2.23)}$$

・Equation of State for Density

$$\rho = \rho(S, T) \quad \text{Eq. (2.24)}$$

・Transport Equations for Salinity and Heat

$$\frac{\partial S}{\partial t} + (\boldsymbol{v} \cdot \nabla) \cdot S = \nabla \cdot \boldsymbol{F}_S \qquad \text{Eq. (2.25)}$$

$$\frac{\partial T}{\partial t} + (\boldsymbol{v} \cdot \nabla) \cdot T = \nabla \cdot \boldsymbol{F}_T \qquad \text{Eq. (2.26)}$$

Where x, y, and z are the horizontal (x, y) and vertical (z) coordinates (positive upward), t is time, $\boldsymbol{v}$ is the velocity vector $\boldsymbol{v} = (U, V, W)$; U, V, and W are the velocity components in the x, y, z directions, p is the pressure, ρ is the density, $\boldsymbol{\tau}_{xx}$, $\boldsymbol{\tau}_{yx}$, *etc.* are the shear stress, f is the Coriolis parameter, g is the gravitational acceleration, S is the salinity, T is the water temperature, $\boldsymbol{F}_S$ is the turbulent diffusion flux of salinity, and $\boldsymbol{F}_T$ is the turbulent diffusion flux of temperature.

Models that use the fundamental equations presented so far are called pure 3D models or Full3D models, in the sense that they can calculate complete 3D flow and pressure fields without any assumptions. In this case, solving for the physical quantities of the flow results in extremely high computational costs. Therefore, a hydrostatic pressure distribution was assumed. In other words, in coastal areas, the horizontal scale (approximately 10 to 100 km) is overwhelmingly larger than the water depth (approximately 10 to 100 m), and the time scale of physical phenomena is large (several hours to tens of hours), so the vertical acceleration term and (eddy) viscosity term are extremely small compared to the gravity term. Moreover, Boussinesq approximation was also assumed. As a result, the horizontal component of the equation of motion can be rewritten as shown in Eq. (2.27) and Eq. (2.28).

$$\frac{\partial U}{\partial t} + (\boldsymbol{v} \cdot \nabla) \cdot U - fV = -\frac{1}{\rho_0}\frac{\partial p}{\partial x} + \frac{1}{\rho_0}\left(\frac{\partial}{\partial x}\tau_{xx} + \frac{\partial}{\partial y}\tau_{yx} + \frac{\partial}{\partial z}\tau_{zx}\right) \qquad \text{Eq. (2.27)}$$

$$\frac{\partial V}{\partial t} + (\boldsymbol{v} \cdot \nabla) \cdot V + fU = -\frac{1}{\rho_0}\frac{\partial p}{\partial y} + \frac{1}{\rho_0}\left(\frac{\partial}{\partial x}\tau_{xy} + \frac{\partial}{\partial y}\tau_{yy} + \frac{\partial}{\partial z}\tau_{zy}\right) \qquad \text{Eq. (2.28)}$$

Furthermore, since the change in density is small, the continuity equation can be rewritten as shown in Eq. (2.29).

$$\nabla \cdot \mathbf{v} = 0 \qquad \text{Eq. (2.29)}$$

2.7.3 Turbulence closure modeling

To solve the Reynolds-Averaged Navier-Stokes (RANS) equations, a turbulence closure model was employed. The primary objective of this modeling was to close the system of equations by expressing the unknown Reynolds stress terms—which arise from the averaging process—using known mean flow variables.

In this study, the eddy viscosity concept was adopted, where turbulent transport was approximated as an enhanced molecular viscosity. Since the computational grid cannot resolve all micro-scale turbulent eddies, these sub-grid scale effects were parameterized using an eddy viscosity coefficient. This approach ensured that the number of equations matched the number of variables, allowing for a stable numerical solution of the fluid motion.

2.7.4 Heat flux model

Several heat flux models are available in Delft3D-FLOW. In this study, Murakami heat flux model (Murakami *et al.*, 1985) was selected. The fomulation of the heat flux is presented in Eq. (2.30). A distinctive feature of the Murakami model is that the latent heat (evaporative) flux has been specifically calibrated for Japanese coastal waters, such as the Seto Inland Sea.

In this model, time-series data of relative humidity, temperature, and solar radiation must beprovided as input. In additon, parameters such as sky cloudiness, Secchi depth, and the Dalton number can be specified by the user. Increasing the sky cloudiness parameter reduces daytime heating. However, the imported solar radiation data may already account for cloud effects, careful consideration is required to avoid double couting.

Secchi depth is used to estimate the light extinction coefficient. A smaller Secchi depth results in stronger light attenuation, causing surface water temperature to increase more easily. The Dalton number represents the bulk transfer coefficient governing evaporative heat loss. A larger Dalton number enhances evaporative cooling and consequently lowers the water temperature.

$$Q_{tot} = Q_{sn} + Q_{an} - Q_{br} - Q_{ev} - Q_{co} \qquad \text{Eq. (2.30)}$$

Where Q_{tot} is the solar radiation (Short-wave radiation) (W/m^2), Q_{sr} is the reflected solar radiation (W/m^2), Q_{sn} is the net solar radiation ($Q_{tot} = Q_s - Q_{sr}$) (W/m2), Q_a is the atmospheric radiation (Long-wave radiation) (W/m^2), Q_{ar} is the reflected atmospheric radiation (W/m^2), Q_{an} is the net atmospheric radiation ($Q_{an} = Q_a - Q_{ar}$) (W/m^2), Q_{br} is the back radiation (Terrestrial radiation) (W/m^2), Q_{ev} is the latent heat flux (Evaporative heat transport) (W/m^2), and Q_{co} is the sensible heat flux (Conduction/Convection heat transport) (W/m^2).

2.7.5 Computational grid

In this model, different coordinate systems were applied to the horizontal and vertical directions. A Cartesian coordinate system was applied to the horizontal grid, and the σ coordinate system was applied to the vertical direction. For the linear Cartesian coordinate system (x, y, z, t), the σ coordinate system was transformed as shown in Eq. (2.31).

$$x^* = x,\ y^* = y,\ t^* = t,\ \sigma = \frac{z-\eta(x,y,t)}{H(x,y)+\eta(x,y,t)} = \frac{z-\eta}{D} \qquad \text{Eq. (2.31)}$$

Where η is the tide level (deviation from the mean water level MWL), H is the mean water depth, D is the total water depth.

The z-axis is defined vertically upward. If z = 0 at the mean water level, then σ = 0 at the water surface ($z = -H$) and $\sigma = -1$ at the seabed ($z = -H$). **Figure 2.14** shows the relationship between the linear Cartesian coordinate system and the σ coordinate system.

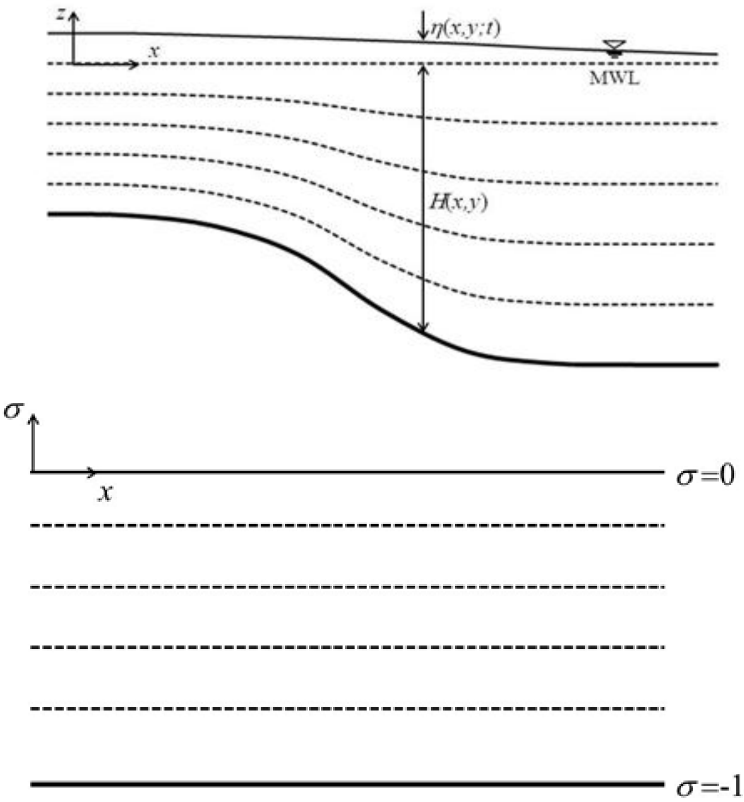

Fig. 2.14 Relationship between the cartesian coordinate system and the σ coordinate system

Consequently, the final equation of motion in the x-direction for the σ-coordinate system was expressed as Eq. (2.32). The equations of motion in the y-direction and the transport equations for scalar quantities S and T were derived through a similar procedure.

$$\frac{\partial DU}{\partial t}+\frac{\partial DU^2}{\partial x}+\frac{\partial DUV}{\partial y}+\frac{\partial U\omega}{\partial \sigma}-fDV = -gD\frac{\partial \eta}{\partial x}-\frac{gD^2}{\rho_0}\int_{\sigma}^{0}\left(\frac{\partial \rho'}{\partial x}-\frac{\sigma}{D}\frac{\partial D}{\partial x}\frac{\partial \rho'}{\partial \sigma}\right)d\sigma + \frac{\partial}{\partial x}\left(2D\nu_{tH}\frac{\partial U}{\partial x}\right)+\frac{\partial}{\partial y}\left\{D\nu_{tH}\left(\frac{\partial U}{\partial y}+\frac{\partial V}{\partial x}\right)\right\}+\frac{\partial}{\partial \sigma}\left(\frac{\nu_{tV}}{D}\frac{\partial U}{\partial \sigma}\right) \quad \text{Eq. (2.32)}$$

2.8 Low Trophic Level Ecosystem Model (LTLE Model)

This section describes the Low Trophic Level Ecosystem Model (LTLE Model). Delft3D-WAQ was employed to improve the existing LTLE model. Delft3D-WAQ is a module designed for water quality and aquatic ecology modeling. All ecological calculations were performed based on the results obtained from the Flow Model. For example, salinity, water temperature, and water velocity were used. Therefore, the computational domain, resolution, the number of vertical layers in σ coordinate system, river inflow locations, and discharges were identical to those used in the Flow Model.

LTLE Model was originally developed by Komori *et al*. (2021). By indicated by its name, the model focuses exclusively on lower trophic levels; only phytoplankton are taken into account while higher trophic organisms such as zooplankton and seagrass were not included in the original model. **Figure 2.15** illustrates the model compartments and their interactions. The original LTLE Model consists of phytoplankton (one species), three types of inorganic nutrients, particle organic matter (POM), dissolved oxygen (DO), DIC, and TA. The processes represented in the model include photosynthesis, respiration, mortality, settling and decomposition of organic matter, nitrification, and reaeration.

Generally, it is common to incorporate multiple phytoplankton functional types, but only a single type was considered in this model for simplicity (Komori *et al*., 2021). Moreover, dissolved organic matter (DOM) was not included because it was assumed that DOM was decomposed faster than POM, and DOM changed to inorganic nutrients.

In this study, one species of seagrass was incorporated into the original LTLE Model. To maintain model simplicity, only two additional processes were introduced: photosynthesis and respiration of seagrass. Delft3D-WAQ provedes a number of predefined ecological processes, including photosynthesis and respiration of phytoplankton. While photosynthesis of submerged macrophytes such as seagrass is available in Delft3D-WAQ, their respiration is not explicitly modeled. Therefore, the LTLE Model was modified by adjusting the phytoplankton respiration parameter to represent seagrass respiration and by specifying parameters related to seagrass photosynthesis.

In addtion, input of inorganic nutrients, suspended organic matter, and DO coming from each river were incorporated into the model. The location of each river was same as the Flow Model. Nutrient loads from rivers were estimated using L-Q equations based on the water quality data from Class A river, obtained from the Ministry of Land, Infrastructure, Transport and Tourism observatory database. Dissolved oxygen concentration in river inflows were calculated by linear interpolation of observational data over time. Model parameters were calibrated with reference to Komori *et al.* (2021) and Tadokoro and Yano. (2019).

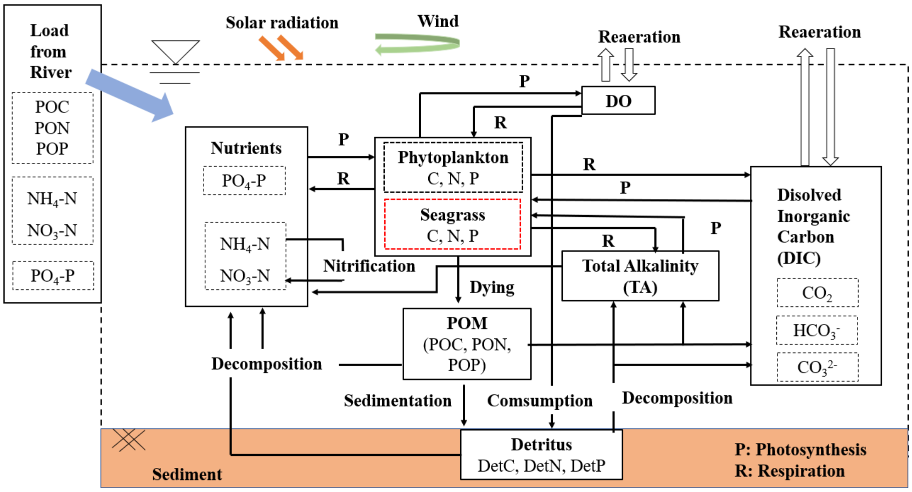

Fig. 2.15 Components and interaction between them

2.8.1 Model equation

Each state variable was described by a three-dimensional mass transport equation, where increases and decreases due to biological processes were incorporated into the source/sink term. The governing equation for a state variable C at any point (x, y, z) within the computational domain was expressed as shown in Eq. (2.33)

$$\frac{\partial C}{\partial t} + (\boldsymbol{v} \cdot \nabla) \cdot C = \nabla \cdot \boldsymbol{F}_C + \left(\frac{\partial C}{\partial t}\right)_{\mathrm{eco}} \qquad \text{Eq. (2.33)}$$

Where $\boldsymbol{F}_{\mathrm{C}}$ is the turbulent diffusion flux of state variable C, and $(\partial C/\partial t)_{\mathrm{eco}}$ is the rate of change due to biological processes.

$(\partial C/\partial t)_{\mathrm{eco}}$ needs to be expressed as equation for each process, and Eq. (2.34) to Eq. (2.40) are model equations for each process.

$$\left(\frac{\partial C_{ALG}}{\partial t}\right)_{\text{eco}} = B_{\text{gro},C} - B_{\text{mor},C} \quad \text{Eq. (2.34)}$$

$$\left(\frac{\partial C_{MAC}}{\partial t}\right)_{\text{eco}} = B_{\text{MACgro},C} \quad \text{Eq. (2.35)}$$

$$\left(\frac{\partial C_{POM}}{\partial t}\right)_{\text{eco}} = B_{\text{mor},M} - B_{\text{dec},\,M} - B_{\text{set},\,M} + q_{POM} \quad \text{Eq. (2.36)}$$

$$\left(\frac{\partial C_{NH_4}}{\partial t}\right)_{\text{eco}} = B_{\text{dec},N} + B_{\text{aut},N} + B_{\text{mel},N} - B_{\text{nit}} - B_{\text{gro},NH_4} + q_{NH_4} \quad \text{Eq. (2.37)}$$

$$\left(\frac{\partial C_{NO_3}}{\partial t}\right)_{\text{eco}} = B_{\text{nit}} - B_{\text{gro},NO_3} + q_{NO_3} \quad \text{Eq. (2.38)}$$

$$\left(\frac{\partial C_{PO_4}}{\partial t}\right)_{\text{eco}} = B_{\text{dec},P} + B_{\text{aut},P} + B_{\text{mel},P} - B_{\text{gro},P} + q_{PO_4} \quad \text{Eq. (2.39)}$$

$$\left(\frac{\partial C_{DO}}{\partial t}\right)_{\text{eco}} = D_{\text{rea}} + D_{\text{gro}} - D_{\text{dec}} - D_{\text{nit}} - D_{\text{sod}} + q_{DO} \quad \text{Eq. (2.40)}$$

Where q_i is the external loading from outside the system.

Subscripts:

gro: Net growth of phytoplankton, mor: Mortality of phytoplankton, MAC.gro: Net growth of seagrass, dec: Decomposition of particulate organic matter, set: Settling, aut: Nutrient release due to mortality, mel: Release from bottom sediments, nit: Nitrification, rea: Reaeration, sod: Sediment oxygen demand

Each equation is explained in following section. Especially, seagrass biological processes are mainly explained because this study focuses on improving the exiting model by incorporating seagrass. Most of processes were based on Delft3D manuals. For details of model explanation, refer to the manuals (Deltares, 2018). Each parameter and constant used in previous studies is listed in **Table A1**, Appendix A. Moreover, parameters and constants added or modified in this study are shown in **Table A2**, Appendix.

2.8.2 Seagrass

Generally, the net growth rate of submerged macrophytes (name of Delft3D compartment), $B_{\mathrm{MACgro},C}$ was expressed as the difference between the growth due to photosynthesis ($B_{\mathrm{MACgpp},C}$) and the loss due to respiration ($B_{\mathrm{MACrsp},C}$) as shown in Eq. (2.41) and Eq. (2.42). However, the respiration process of submerged macrophytes is not provided in Delft3D-WAQ. On the other hand, Delft3D-WAQ provides phytoplankton respiration process. Therefore, it was assumed that the respiration process of submerged macrophytes was same as that of phytoplankton, and seagrass respiration was expressed by adjusting a parameter of phytoplankton respiration.

Photosynthesis process of submerged macrophytes ws explained in this section, and the respiration process was done in next section. In Delft3D-WAQ, mortality process of submerged macrophytes is available; however, it was not included in this study in order to simplify the model structure. Furthermore, the simulation were conducted for May and June, assuming that eelgrass continued to grow throughout this period. Note that the respiration of seagrass, $B_{MAC,rsp,C}$ was expressed by the respiration of phytoplankton. For the sake of convenience, it was described here.

$$B_{\mathrm{MAC,gro},C} = B_{\mathrm{MAC,gpp},C} - B_{\mathrm{MAC,rsp},C} \qquad \text{Eq. (2.41)}$$

$$B_{\mathrm{MAC,gpp},C} = \left\{\alpha_1 \times f_{temp} \times f_{nut} \times f_{rad}\right\} \cdot C_{MAC} \qquad \text{Eq. (2.42)}$$

Where α_1 is the potential growth rate of seagrass (/d), f_{temp} is the photosynthetic limitation factor due to water temperature, f_{nut} is the photosynthetic limitation factor due to nutrient availability, f_{rad} is the photosynthetic limitation factor due to radiation, and C_{MAC} is the biomass of seagrass (gC/m^2).

1. Limitation due to water temperature

Water temperature limitation factor, f_{temp} was calculated using Eq. (2.43) and Eq. (2.44). Basically, 20 degrees was the baseline, and growth of submerged macrophytes was promoted when the ambient water temperature was larger than 20. Conversely, if it was less than 20, the growth was suppressed. In addition to that, critical temperature was set in Delft3D-WAQ, and the growth wa totally stopped when the ambient water temperature was less than the critical temperature.

$$f_{temp} = {\beta_1}^{(T-20)} \ (if\ T > T_{crit}) \qquad \text{Eq. (2.43)}$$

$$f_{temp} = 0 \ (if\ T \leq T_{crit}) \qquad \text{Eq. (2.44)}$$

Where β_1 is the temperature coefficient for growth, T is the water temperature (^oC), and T_{crit} is the critical water temperature for growth (^oC).

2. Limitation due to nutrients

The nutrient limitation factor, f_{nut}, was calculated using Eq. (2.45) to Eq. (2.48), based on Liebig's Law of the Minimum (Nakata, 1993). In this approach, the growth rate was determined by the most limiting nutrient, typically the minimum value among the limitation factors for nitrogen and phosphorus. Limitation of nitrogen was determined by concentration of ammonia and nitrate. Specifically, stricter factor was selected by the minimum of phosphorus and nitrogen (the maximum of ammonia and nitrate). Monod equation includes half-saturation constant, and it can be edited by users. When this value is smaller, submerged macrophytes can grow easily.

$$f_{nut} = min(f_{PO4}, \max\ (f_{NH4}, f_{NO3})) \qquad \text{Eq. (2.45)}$$

$$f_{NH4} = \frac{NH4}{NH4 + NH4hs} \qquad \text{Eq. (2.46)}$$

$$f_{NO3} = \frac{NO3}{NO3 + NO3hs} \qquad \text{Eq. (2.47)}$$

$$f_{PO4} = \frac{PO4}{PO4 + PO4hs} \qquad \text{Eq. (2.48)}$$

Where f_{NH4} is the ammonium limitation factor, f_{NO3} is the nitrate limitation factor, f_{PO4} is the phosphorus limitation factor, and hs is the half-saturation constant.

3. Limitation due to light intensity

The radiation limitation factor, f_{rad} was calculated using Eq. (2.49), based on the light intensity at the tip of submerged macrophytes. This equation was adapted when the light intensity at the tip of submerged macrophytes was less than the saturation light intensity. When the light intensity was larger than the saturation light intensity, the radiation limitation factor remains 1.0, which means that growth of seagrass is not surpassed due to too strong light.

$$f_{rad} = \min(1, \frac{Itop_n}{I_{sat}}) \quad \text{Eq. (2.49)}$$

Where $Itop_n$ is the light intensity at the tip of submerged macrophytes in Layer N (W/m^2), and I_{sat} is the light intensity at which saturation take places for submerged macrophytes (W/m^2).

In this approach, light attenuation from the water surface to the bottom was considered. When emerged macrophytes exist, they also attenuate the light intensity. However, emerged macrophytes were not considered in this study because eelgrass cannot grow above the water surface. The light intensity in water was attenuated exponentially by water itself, suspended matter, and submerged macrophytes, obeying Lambert-Beer law, and it was expressed as extinction coefficient. **Fig. 2.16** shows the light intensity attenuation in water. For example, growth of submerged macrophytes in Layer N was simulated based on the light intensity at the top of Layer N, $Itop_n$. Then, $Ibot_n$ was calculated based on the extinction coefficient of Layer N from Z_{n-1} to Z_n. The light intensity was calculated in the subsequent layers.

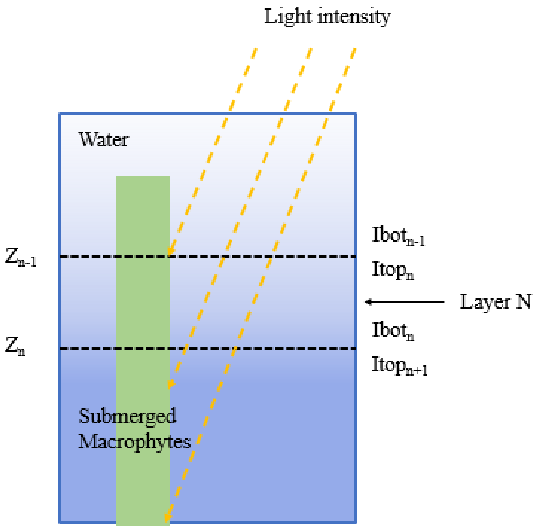

Fig. 2.16 Light intensity attenuation in water

2.8.3 Location of eelgrass

To accurately simulate pCO_2 dynamics, it was necessary to specify the spatial distribution of seagrass within the Delft3D-WAQ computational domain. Accordingly, a spatial input file defining the locations of seagrass was incorporated into the model.

Delft3D-WAQ includes a process defined as the Habitat Suitability Index (HSI), which ranges from 0.0 to 1.0. An HSI value of 0.0 indicates that environmental conditions are unsuitable for seagrass survival and growth, whereas a value of 1.0 represents optimal habitat conditions. In this study, the HSI approach was applied to define the seagrass distribution.

Fig. 2.17 presents the HSI file used in the model, where red indicates an HSI value of 1.0 and blue indicates 0.0. An HSI value of 1.0 was assigned to six grid nodes corresponding to the observation sites, while all other grid nodes were assigned a value of 0.0.

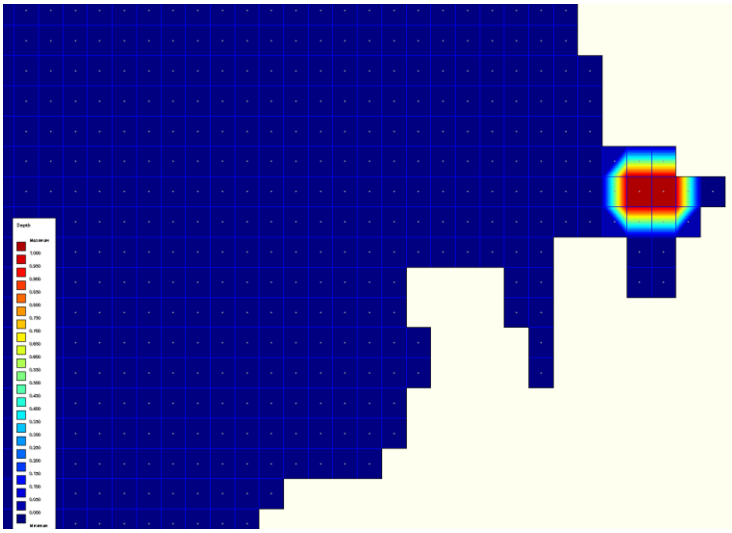

Fig. 2.17 Values of habitat suitability index for seagrass

2.8.4 Phytoplankton

In this section, the processes related to phytoplankton are explained. As mentioned in Section 2.8.2, the submerged macrophytes respiration process is also explained here.

The net growth rate of phytoplankton, $B_{\mathrm{gro},C}$ was expressed as the difference between the growth due to photosynthesis ($B_{\mathrm{gpp},C}$) and the loss due to respiration ($B_{\mathrm{rsp},C}$) as shown in Eq. (2.50) to Eq. (2.53). The form of equations is same as that of submerged macrophytes, and photosynthesis process was determined by the limitation factors of the ambient water temperature, nutrient, and light intensity. Therefore, only the differences from submerged macrophytes is described here.

$$B_{\mathrm{gro},C} = B_{\mathrm{gpp},C} - B_{\mathrm{rsp},C} \qquad \text{Eq. (2.50)}$$

$$B_{\mathrm{gpp},C} = \left\{\alpha_2 \cdot {\beta_2}^{(T-20)} \cdot \mu_{\mathrm{nut}} \cdot \mu_{\mathrm{lt}}\right\} \cdot C_{ALG} \qquad \text{Eq. (2.51)}$$

$$B_{\mathrm{rsp},C} = \left\{\alpha_3 \cdot {\beta_3}^{(T-20)}\right\} \cdot C_{ALG} \qquad \text{Eq. (2.52)}$$

$$B_{\mathrm{mor},C} = \left\{\alpha_4 \cdot {\beta_4}^{(T-20)}\right\} \cdot C_{ALG} \qquad \text{Eq. (2.53)}$$

Where α_2 is the maximum growth rate at 20°C (1/d), β_2 is the temperature coefficient for growth, μ_{nut} is the photosynthetic limitation factor for phytoplankton due to nutrient availability, μ_{lt} is the photosynthetic limitation factor for phytoplankton due to light intensity, C_{ALG} is the biomass of phytoplankton (gC/m^3), α_3 is the respiration rate at 20°C (1/d), β_3 is the temperature coefficient for respiration, α_4 is the mortality rate at 20°C (1/d), and β_4 is the temperature coefficient for mortality.

1. Limitation due to nutrient

The nutrient limitation factor, μ_{nut}, was also determined based on Liebig's Law of the Minimum (Nakata, 1993) in the same way as submerged macrophytes as shown in Eq. (2.54).

$$\mu_{\mathrm{nut}} = min\left(\frac{C_N}{K_{s,N} + C_N}, \frac{C_P}{K_{s,P} + C_P}\right) \qquad \text{Eq. (2.54)}$$

Where C_N is the concentration of nitrate, C_P is the concentration of phosphorus, and $K_{s,i}$ is the half-saturation constant.

2. Limitation due to light intensity

The radiation limitation factor, μ_{lt} was calculated based on the average light intensity in each layer. In this approach, light attenuation from the water surface to the bottom was considered as shown in Eq. (2.55). This equation was adapted when the light intensity at the water surface was less than the optimum light intensity. When the light intensity at the surface was larger than the optimum light intensity, the radiation limitation factor remains 1.0, which means that growth of phytoplankton was not surpassed due to too strong light.

$$\mu_{\mathrm{lt}} = \frac{I_s}{I_o}\frac{1 - e^{-et\times H}}{et \times H} \qquad \text{Eq. (2.55)}$$

Where I_s is the light intensity at the water surface (W/m^2), I_o is the optimum light intensity (W/m^2), *et* is the light extinction (1/m), and *H* is the depth from the surface (m).

3. Respiration

Organic matter produced through photosynthesis was consumed by respiration. In this model, respiration was assumed to be a function of water temperature only, as expressed in Eq. (2.52). Originally, maintenance respiration was considered in the existing model, and the coefficient was modified to expressed the influence of seagrass because Delft3D-WAQ does not provide respiration process of submerged macrophytes. Specifically, the value was estimated based on the ratio of eelgrass biomass to phytoplankton biomass. There is few research on clarifying the biomass of eelgrass clearly. Therefore, it was estimated from dry weight of eelgrass and the ratio of carbon to the dry weight. Dry weight of eelgrass varies with research, distributed area, and season. In this study, with reference to Suzuki (1997) and Komatsu *et al*. (2006), the dry weight of eelgrass was about 0.3 to 0.8 kg DW/m^2. These values were multiplied by the carbon content rate per the dry weight, 0.3 to 0.4 gC/gDW. As a result, the biomass of eelgrass was 90 to 320 gC/m^2. Based on visual observations, the maximum canopy height of eelgrass was estimated to be approximately 1 m. Accordingly, the biomass per unit volume was estimated to range from 90 to 320 gC/m^3.

The biomass of phytoplankton also varies with time and place. According to the results of Komori *et al*. (2021), the biomass was about 0.6 to 0.9 gC/m^3 under the mixed condition. Given the biomass of eelgrass was 90 to 320 gC/m^3, the ratio of the biomass was 100 to 530. The respiration rate of eelgrass was expressed by applying this ratio to the respiration rate of phytoplankton. The phytoplankton respiration rate in the original model was 0.041 (1/d). This value was multiplied by the biomass ratio, resulting in a respiration rate ranging fro 4.1 (1/d) to 21.7 (1/d).

4. Morality

Mortality is fundamentally a process of phytoplankton biomass decline due to cellular senescence. This model assumed a functional form that depends solely on water temperature

2.8.5 Other compartments and processes

In this study, the existing model was improved by adding the seagrass processes, which meant that other compartments and processes were basically same as Komori *et al*. (2021). Therefore, detailed explanation is not described in this study, refer to Komori *et al*. (2021).

1. Particulate organic matter

The dynamics of particulate organic matter (POM) are governed by three primary processes: mortality of phytoplankton, decomposition, and settling.

2. inorganic nutrients

The inorganic nutrient compartments consist of three components: ammonium, nitrate, and phosphate. The relevant biogeochemical processes included uptake by phytoplankton and submerged macrophytes, release of nutrients due to mortality, decomposition of organic matter, sediment release, and nitrification.

3. Dissolved oxygen

The dissolved oxygen (DO) dynamics were governed by five primary processes: reaeration, photosynthetic and submerged macrophytes production, consumption by organic matter decomposition, nitrification, and sediment oxygen demand (SOD).

4. Dissolved inorganic carbon

Dissolved inorganic carbon (DIC) dynamics were governed by four primary processes: photosynthesis, respiration, mineralization of POM and detritus, and reaeration.

5. Total alkalinity (TA)

Total alkalinity dynamics were governed by three primary processes: photosynthesis, respiration, nitrification, and mineralization of POM and detritus.

2.8.6 Load of nutrient

To estimate nutrient loading from rivers, which contributes a critical boundary condition for the LTLE Model, load estimation equations were developed. Although water quality monitoring is conducted for Class A rivers, continuous measurements—such as water level and discharge records—are not always available at the same locations as the water quality monitoring stations.

In this study, nutrient load equations were formulated using the L-Q equation in shown in Eq. (2.56), a widely used empirical approach for estimating water quality parameters, following Tadokoro and Yano (2019). The analysis included eight Class A rivers: seven rivers discharging into the Ariake Sea (the Rokkaku River, the Kase River, the Chikugo River, the Yabe River, the Kikuchi River, the Shira River, and the Midori River; excluding the Honmyo River) and the Kuma River River, which flows into the Yatsushiro Sea.

Table 2.4 lists the discharge and water quality monitoring stations for each river, and their geographical locations are presented in **Fig. 2.18**. For each river, the discharge monitoring station was selected to minimize its distance from the corresponding water quality station. Nutrient loads were then calculated using the parameters a and b derived by Tadokoro *et al*. (2019) The specific values of these parameters are provided in **Table 2.5.**

$$L = a \cdot Q^b \qquad \text{Eq. (2.56)}$$

Where L is the load of nutrient (g/m^3), Q is the discharge of rivers (m^3/s), and a and b are parameters.

Table 2.4 Observatory for discharge and water quality

River	Observatory for discharge	Observatory for water quality
Chikugo	Senoshita	Senoshita
Yabe	Funagoya	Funagoya
Kase	Ikemori	Kanjinbashi
Rokkaku	Myokenbashi	Hazamazeki
Kikuchi	Yamaga	Yamaga
Shira	Yotsugibashi	Yotsugibashi
Midori	Jonan	Jonan
Kuma	Yokoishi	Yokoishi

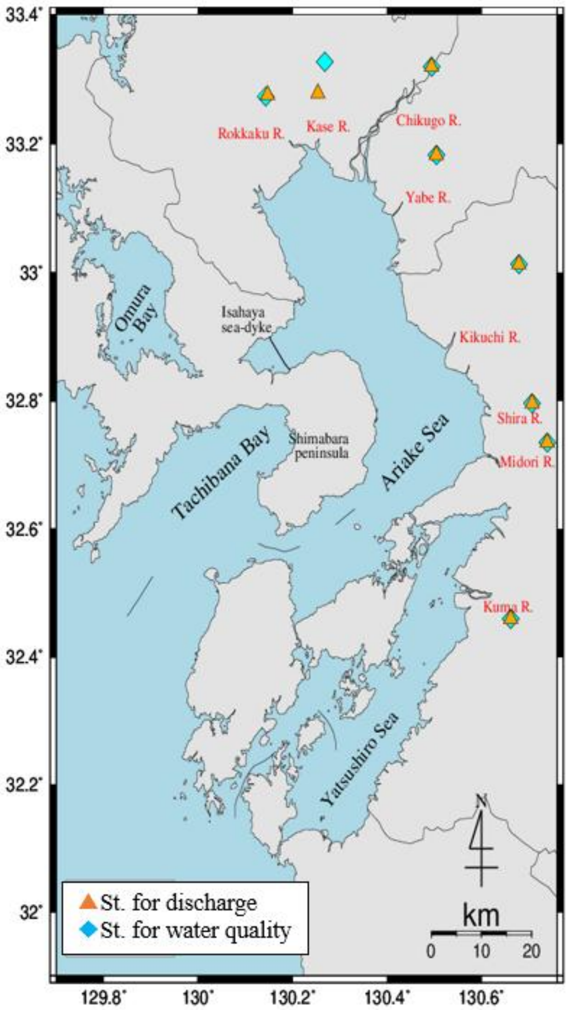

Fig. 2.18 Location of observatory for discharge and water quality

Table 2.5 Parameters for L-Q equation

River		NH_4	NO_3	PO_4	POC	PON	POP
Chikugo	*a*	3.26E-02	1.39E-01	9.16E-03	2.93E-01	5.58E-02	1.98E-03
	b	1.93E-01	4.35E-01	2.97E-01	2.81E-01	1.78E-01	4.40E-01
Yabe	*a*	3.62E-02	1.23E+00	1.45E-02	6.87E-01	1.04E-01	6.48E-03
	b	-6.64E-02	5.33E-02	2.31E-01	1.76E-02	1.76E-02	1.75E-02
Kase	*a*	1.97E-02	4.66E-01	1.67E-02	1.64E-01	4.94E-02	1.42E-02
	b	-1.70E-02	-1.70E-02	-4.33E-01	3.41E-02	4.76E-01	4.46E-01
Rokkaku	*a*	9.18E-02	9.65E-01	4.78E-02	3.59E-01	6.41E-02	1.76E-02
	b	-7.20E-03	-7.20E-03	4.02E-02	1.54E-17	3.67E-01	3.51E-01
Kikuchi	*a*	1.98E-02	3.40E-01	2.13E-02	2.98E-01	5.46E-02	4.05E-03
	b	4.69E-01	5.14E-01	4.67E-01	5.01E-01	3.89E-01	2.99E-01
Shira	*a*	1.15E-02	2.53E-01	1.80E-02	2.75E-01	5.22E-02	3.90E-03
	b	4.76E-01	5.00E-01	4.22E-01	4.96E-01	3.65E-01	2.56E-01
Midori	*a*	9.76E-03	5.68E-01	7.76E-03	5.81E-01	4.81E-02	3.61E-03
	b	1.99E-01	4.95E-02	2.60E-01	1.95E-02	3.58E-01	2.36E-01
Kuma	*a*	3.30E-03	5.42E-02	5.63E-04	5.21E-02	1.25E-02	4.79E-04
	b	4.39E-01	5.07E-01	8.02E-01	5.09E-01	3.16E-01	5.06E-01

3. Results and Discussion

3.1 Observed and calculated values

Figure 3.1 shows the time series of observed and calculated values for DIC, TA, ΔDIC, ΔTA, salinity, water temperature, pCO_2, CO_2 flux, precipitation, solar radiation, and wind speed on 26–27 June 2021.

In general, ΔDIC becomes negative due to photosynthesis and positive due to respiration. ΔTA becomes negative as a result of calcification associated with skeletal formation by corals and shellfish. A negative CO_2 flux indicates CO_2 uptake from the atmosphere into seawater, whereas a positive flux represents CO_2 release from seawater to the atmosphere.

ΔDIC remained negative throughout the entire period and reached its minimum at 18:00, indicating that photosynthesis was dominant. ΔTA showed a similar decreasing trend. Salinity decreased markedly at 9:00 on 27 June; DIC and TA also decreased at that time, whereas ΔDIC and ΔTA showed no substantial change. This suggests that the observed DIC and TA were primarily driven by salinity variations rather than enhanced biological processes such as seagrass metabolism. Rainfall occurred from around 4:00 to 11:00 on 27 June, which may have contributed to these changes.

At most sites and times, pCO_2 was lower than atmospheric CO_2, and the CO_2 flux was negative, indicating net CO_2 uptake. The flux reached its minimum at 00:00 on 26 June, likely due to the influence of wind speed. During the rainfall event, solar radiation was weak, resulting to near-neutral CO_2 flux conditions.

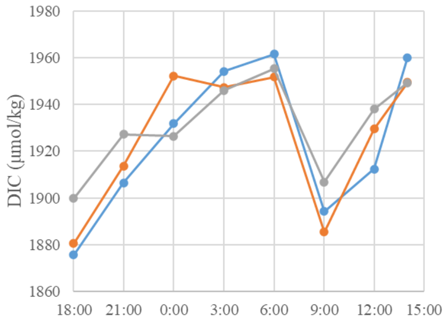
DIC (μmol/kg)
1980
1960
1940
1920
1900
1880
1860
18:00 21:00 0:00 3:00 6:00 9:00 12:00 15:00

(a)

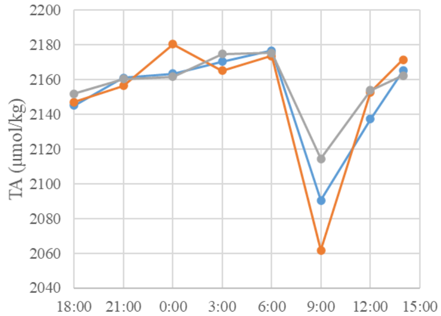
TA (μmol/kg)
2200
2180
2160
2140
2120
2100
2080
2060
2040
18:00 21:00 0:00 3:00 6:00 9:00 12:00 15:00

(b)

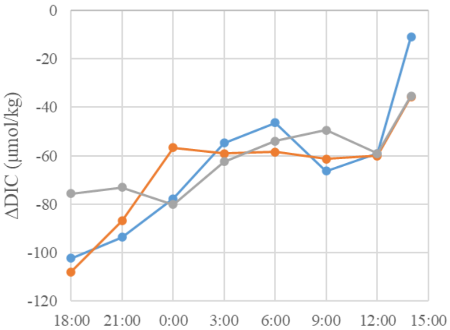
ΔDIC (μmol/kg)
0
-20
-40
-60
-80
-100
-120
18:00 21:00 0:00 3:00 6:00 9:00 12:00 15:00

(c)

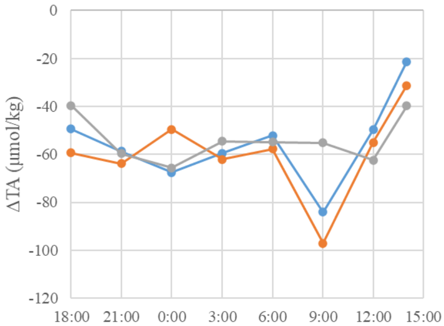
ΔTA (μmol/kg)
0
-20
-40
-60
-80
-100
-120
18:00 21:00 0:00 3:00 6:00 9:00 12:00 15:00

(d)

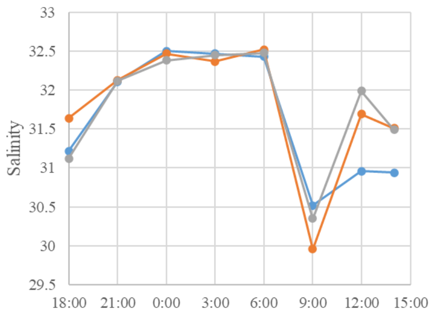
Salinity
33
32.5
32
31.5
31
30.5
30
29.5
18:00 21:00 0:00 3:00 6:00 9:00 12:00 15:00

(e)

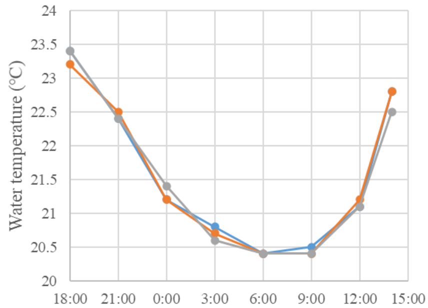
Water temperature (°C)
24
23.5
23
22.5
22
21.5
21
20.5
20
18:00 21:00 0:00 3:00 6:00 9:00 12:00 15:00

(f)

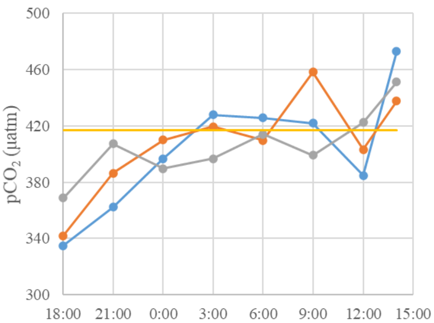
pCO_2 (μatm)
500
460
420
380
340
300
18:00 21:00 0:00 3:00 6:00 9:00 12:00 15:00

(g)

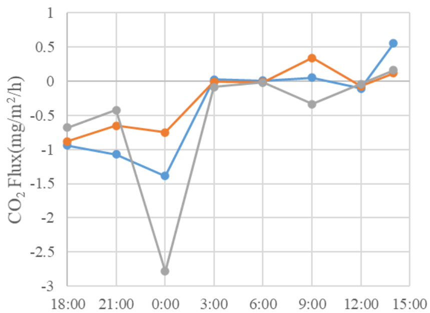
CO_2 Flux(mg/m^2/h)
1
0.5
0
-0.5
-1
-1.5
-2
-2.5
-3
18:00 21:00 0:00 3:00 6:00 9:00 12:00 15:00

(h)

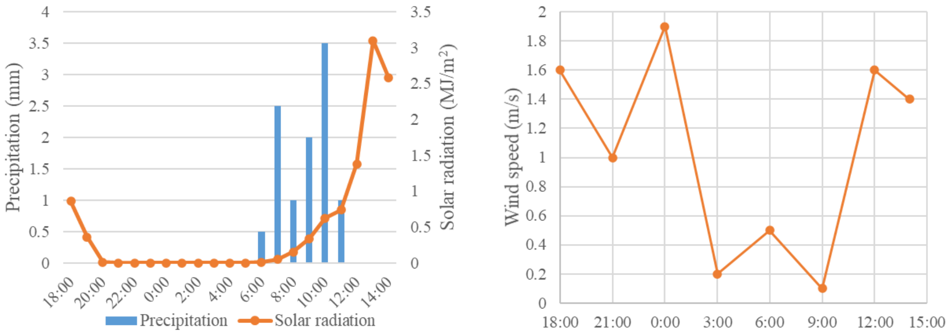

(i) (at St Minamata and St. Kumamoto) (j) (at St Minamata)

Fig. 3.1 Time-series of observed and calculated data on June 26-27, 2021: DIC (a), TA (b), ΔDIC (c), ΔTA (d), salinity (e), water temperature (f), pCO_2 (g), CO_2 flux (h), precipitation at St. Minamata and solar radiation St. Kumamoto (i), and wind speed at St. Minamata (j). (The yellow line indicates atmospheric pCO_2.)

Figure 3.2 shows the time series of observed or calculated values for DIC, TA, ΔDIC, ΔTA, salinity, water temperature, pCO_2, CO_2 flux, precipitation, solar radiation, and wind speed on 10–11 June 2022.

ΔDIC became positive at 03:00 on 10 June and at 15:00 on 11 June; ΔTA exhibited similar behavior. Salinity decreased markedly at 15:00, and DIC and TA were likely influenced by this reduction. The positive values of ΔDIC and ΔTA suggest the dominance of biological processes that increase pCO_2, such as respiration.

Moderate rainfall occurred on 11 June and may have indirectly contributed to the variability in DIC and TA. At all sites and times, pCO_2 remained below atmospheric levels, and the flux was negative, indicating net CO_2 uptake. As observed in 2021, the flux was strongly influenced by wind speed and reached its minimum at 15:00 on 11 June. During this period, cloudy and rainy conditions resulted in weak solar radiation, which may have affected pCO_2 dynamics.

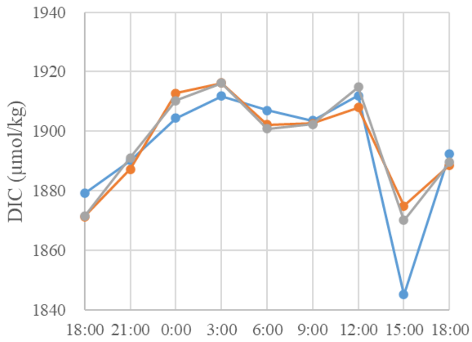
DIC (μmol/kg)
1940
1920
1900
1880
1860
1840
18:00 21:00 0:00 3:00 6:00 9:00 12:00 15:00 18:00

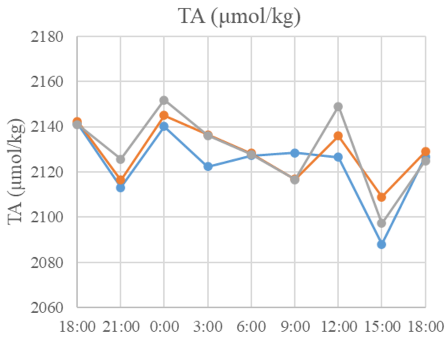
TA (μmol/kg)
TA (μmol/kg)
2180
2160
2140
2120
2100
2080
2060
18:00 21:00 0:00 3:00 6:00 9:00 12:00 15:00 18:00

(a)

(b)

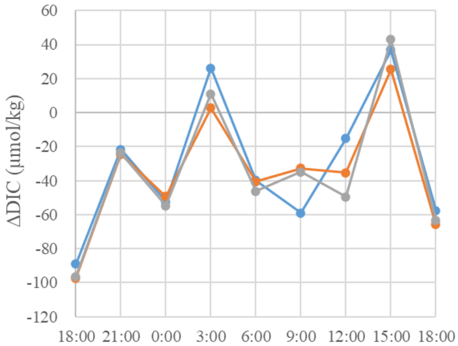
ΔDIC (μmol/kg)
60
40
20
0
-20
-40
-60
-80
-100
-120
18:00 21:00 0:00 3:00 6:00 9:00 12:00 15:00 18:00

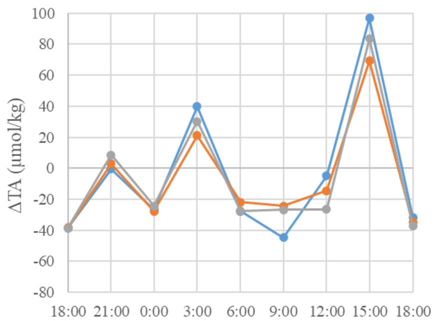
ΔTA (μmol/kg)
100
80
60
40
20
0
-20
-40
-60
-80
18:00 21:00 0:00 3:00 6:00 9:00 12:00 15:00 18:00

(c)

(d)

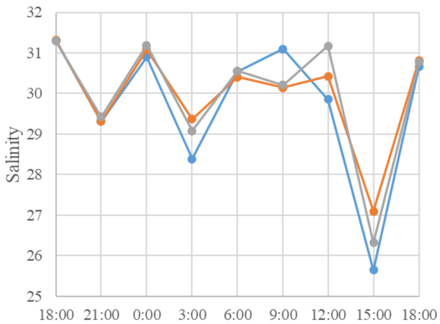
Salinity
32
31
30
29
28
27
26
25
18:00 21:00 0:00 3:00 6:00 9:00 12:00 15:00 18:00

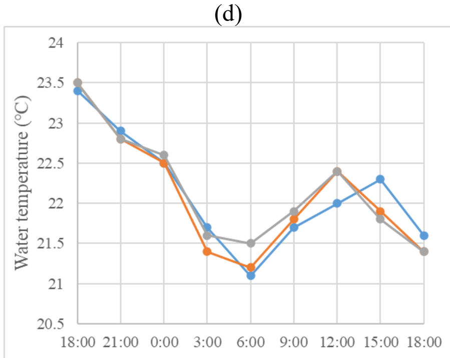
Water temperature (°C)
24
23.5
23
22.5
22
21.5
21
20.5
18:00 21:00 0:00 3:00 6:00 9:00 12:00 15:00 18:00

(e)

(f)

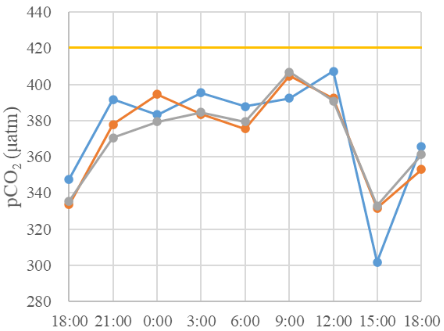
pCO2 (μatm)
440
420
400
380
360
340
320
300
280
18:00 21:00 0:00 3:00 6:00 9:00 12:00 15:00 18:00

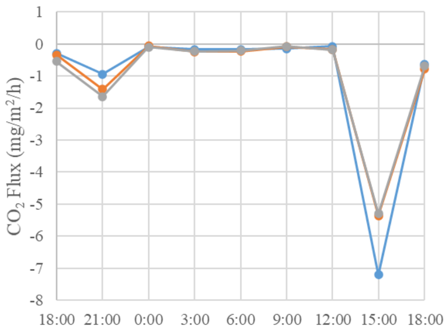
CO2 Flux (mg/m2/h)
1
0
-1
-2
-3
-4
-5
-6
-7
-8
18:00 21:00 0:00 3:00 6:00 9:00 12:00 15:00 18:00

(g)

(h)

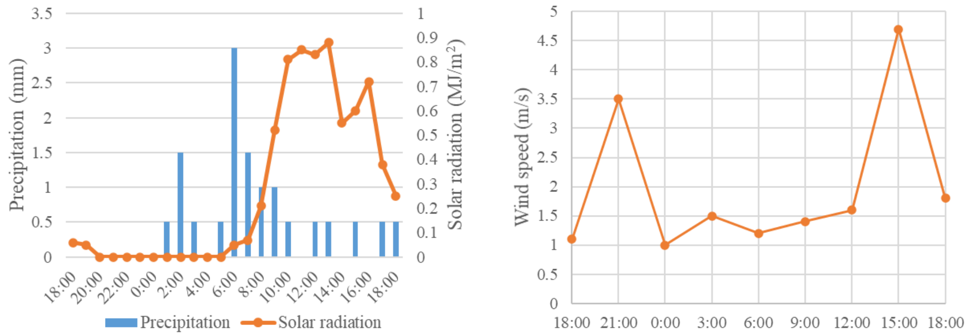

(i) (at St Minamata and St. Kumamoto)　　(j)

St. A　St. B　St. C

Fig. 3.2 Time-series of observed and calculated data on June 10-11, 2022: DIC (a), TA (b), ΔDIC (c), ΔTA (d), salinity (e), water temperature (f), pCO_2 (g), CO_2 flux (h), precipitation at St. Minamata and solar radiation St. Kumamoto (i), and wind speed (j). (The yellow line indicates atmospheric pCO_2.)

Figure 3.3 shows the time series of observed or calculated values for DIC, TA, ΔDIC, ΔTA, salinity, water temperature, pCO_2, CO_2 flux, precipitation, solar radiation, and wind speed on 16–17 May 2023.

ΔDIC was generally negative throughout the period. Because weather conditions remained clear, its absolute magnitude increased during daytime, reflecting enhanced photosynthesis activity. Pronounced differences among observation sites were evident. In particular, DIC and TA at St. C at 13:00 on 17 May exhibited substantially larger variations compared with the other two sites. These differences can be interpreted as follows. At 22:00 on 16 May, salinity decreased, whereas the observed DIC and TA values did not show a corresponding reduction. Since ΔDIC and ΔTA are defined as the differences between the observed DIC and TA and the values calculated from salinity, the apparent variations in ΔDIC and ΔTA reflect the relative magnitudes of changes in salinity-driven changes and the measured DIC and TA responses. The fluctuations observed at 13:00 on 17 May can be interpreted in the same manner.

However, the underlying cause of the distinct variations in DIC and TA at St. C remains unclear, as similar behavior has not been observed in previous surveys. It is uncertain whether these changes were due to anthropogenic influences or to biological activity, such as processes occurring within the seagrass bed.

pCO_2 remained below atmospheric levels throughout the observation period, indicating continuous CO_2 uptake. Compared with 2021 and 2022, the absolute flux values were larger, suggesting enhanced CO_2 absorption. Strong solar radiation during this period likely promoted eelgrass photosynthesis, thereby contributing to the increased CO_2 uptake.

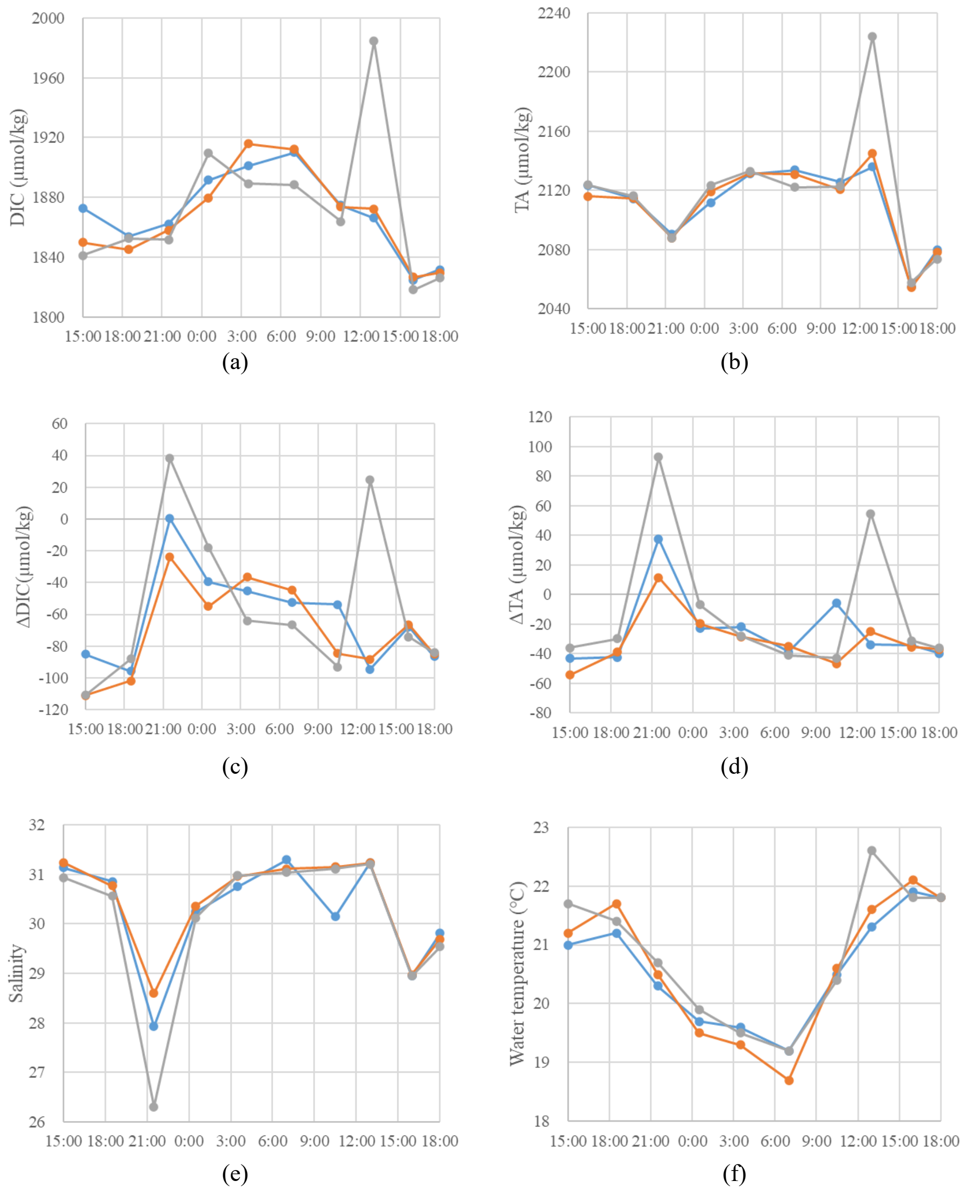

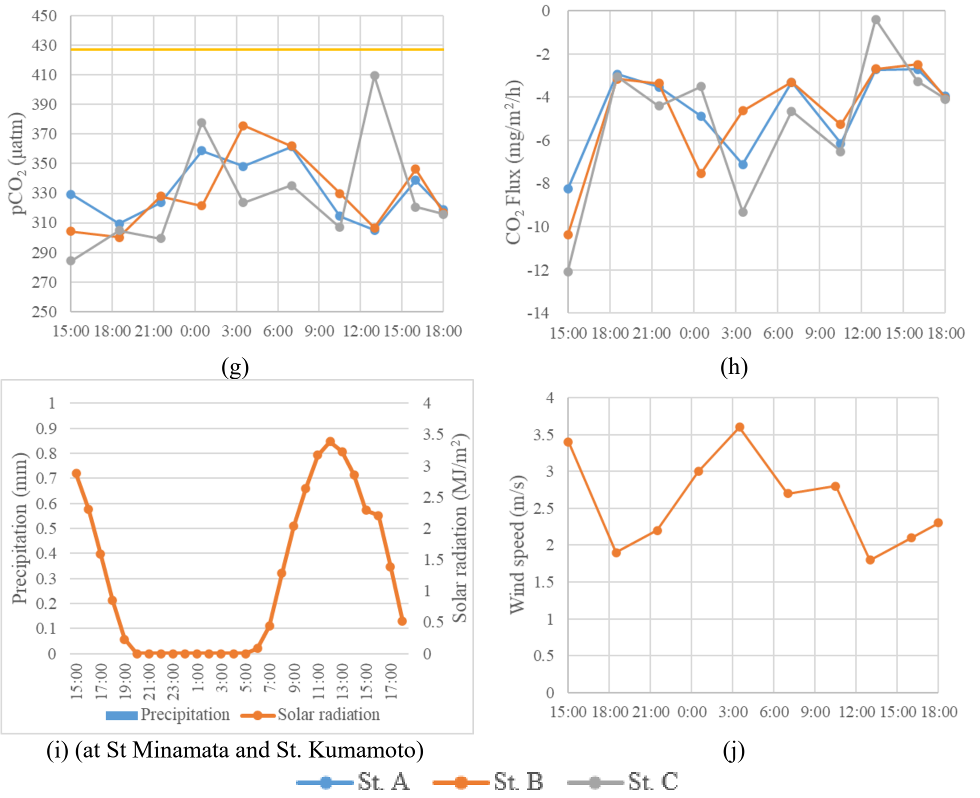

Fig. 3.3 Time-series of observed and calculated data on May 16-17, 2023: DIC (a), TA (b), ΔDIC (c), ΔTA (d), salinity (e), water temperature (f), pCO_2 (g), CO_2 flux (h), precipitation at St. Minamata and solar radiation at St. Kumamoto (i), and wind speed (j). (The yellow line indicates atmospheric pCO_2.)

Figure 3.4 presents the time-series of observed or calculated values for DIC, TA, ΔDIC, ΔTA, salinity, water temperature, pCO_2, CO_2 flux, precipitation, solar radiation, and wind speed on 7–8 June 2024.

At 15:00 on both days, sampling was conducted at low tide under very shallow conditions, and bottom sediments were resuspended, causing strong turbidity that may have significantly influenced DIC and TA. Consequently, pCO_2 may also have been affected. Especially, pCO_2 reached to approximately 470 µatm, which is considerably higher than typical values.

Observations were not conducted between 21:00 and 06:00; therefore, variations during this period remain unknown. Excluding the 15:00 measurements, ΔDIC and CO_2 flux was negative. ΔTA shifted from positive to negative values between 21:00 and 06:00. Salinity showed reduction at 21:00.

Although the weather was cloudy and the solar radiation was weak, pCO_2 was lower than atmospheric CO_2 except at 15:00 on 8 June, when the flux became strongly positive. This anomalous behavior may have been associated with sediment resuspension and increased turbidity during sampling.

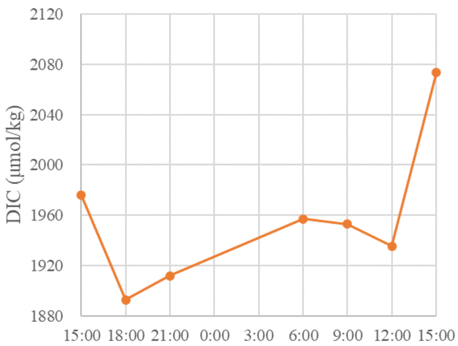

(a)

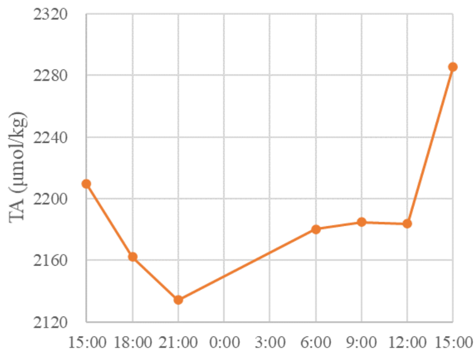

(b)

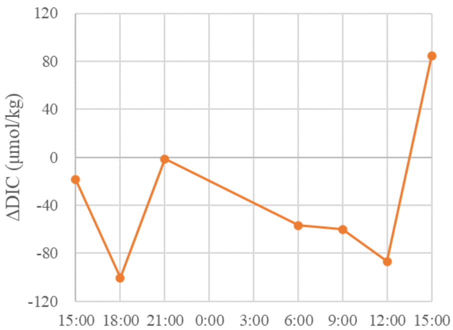

(c)

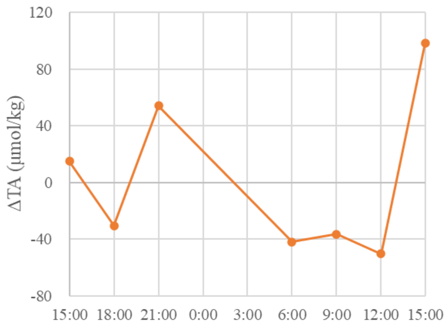

(d)

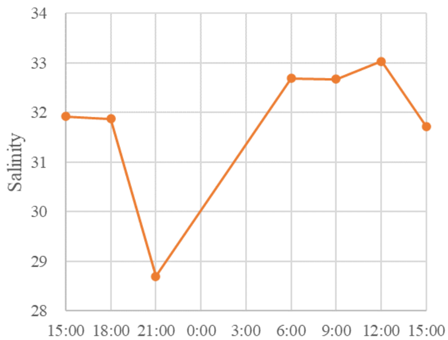

(e)

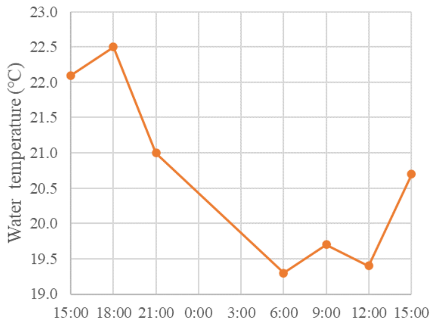

(f)

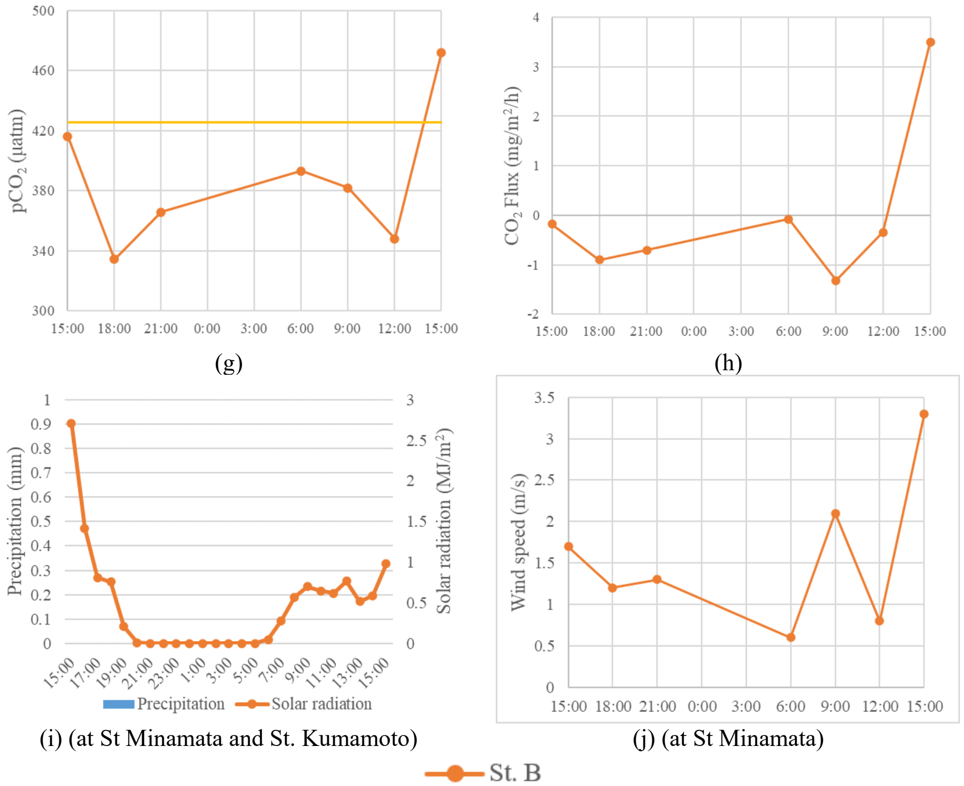

Fig. 3.4 Time-series of observed and calculated data on June 7-8, 2024: DIC (a), TA (b), ΔDIC (c), ΔTA (d), salinity (e), water temperature (f), pCO_2 (g), CO_2 flux (h), precipitation at St. Minamata and solar radiation St. Kumamoto (i), and wind speed at St. Minamata (j). (The yellow line indicates atmospheric pCO_2.)

Figure 3.5 shows the time series of observed or calculated values for DIC, TA, ΔDIC, ΔTA, salinity, water temperature, pCO_2, CO_2 flux, precipitation, solar radiation, and wind speed on 13–14 May 2025.

At 15:00 on 13 May, sampling conducted at low tide caused sediment resuspension and strong turbidity, similar to 2024. ΔDIC and ΔTA shifted from positive to negative values between 21:00 and 06:00. Salinity decreased markedly around 21:00 on 13 May.

ΔDIC on 14 May was likely negative due to enhanced photosynthesis under clear weather conditions, as indicated by strong solar radiation. In contrast, respiration likely dominated at 21:00 on 13 May. Except for the measurement at 15:00 on 13 May, pCO_2 remained below atmospheric levels and the CO_2 flux was negative. The anomaly observed at 15:00 on 13 May may have been influenced by increased turbidity. The flux reached its minimum at 06:00 on 14 May, likely reflecting the influence of wind speed effects.

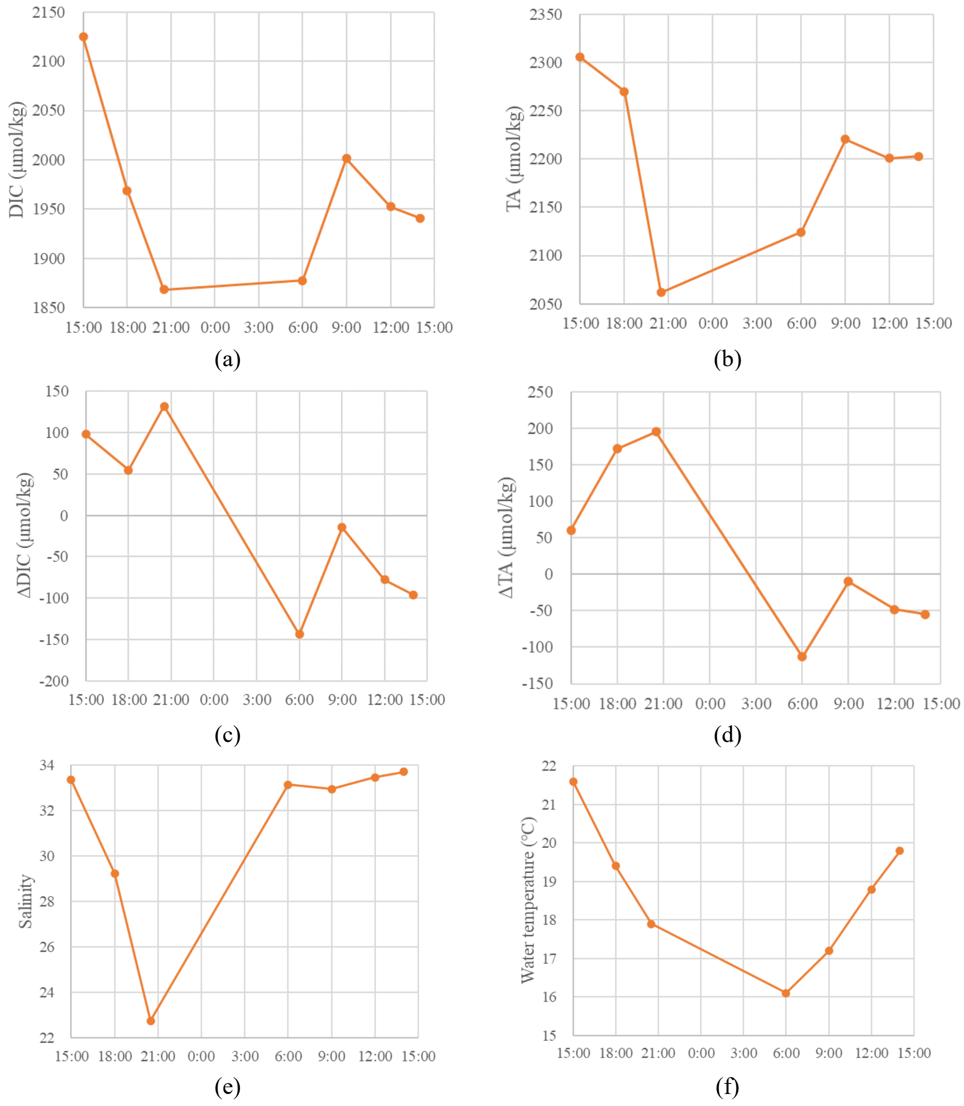

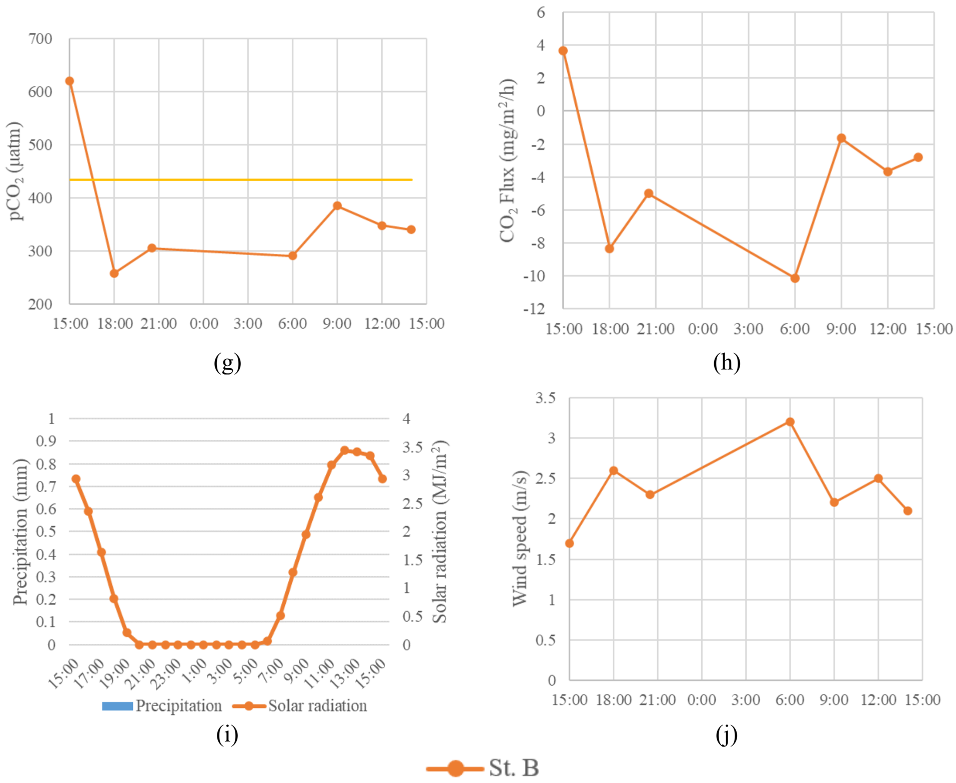

Fig. 3.5 Time-series of observed and calculated data on May 13-14, 2025: DIC (a), TA (b), ΔDIC (c), ΔTA (d), salinity (e), water temperature (f), pCO_2 (g), CO_2 flux (h), precipitation at St. Minamata and solar radiation St. Kumamoto (i), and wind speed (j). (The yellow line indicates atmospheric pCO_2.)

Figure 3.6 presents the time series of observed or calculated values for DIC, TA, ΔDIC, ΔTA, salinity, water temperature, pCO_2, CO_2 flux, precipitation, solar radiation, and wind speed on 19–20 May 2025.

At 12:00 on 19 May, low-tide sampling again caused sediment resuspension and increased turbidity. ΔDIC and ΔTA shifted from positive to negative between 21:00 and 08:00. Both parameters were positive only at 21:00 on 19 May and negative at all other times. Under clear weather conditions, as indicated by strong solar radiation, the effects of daytime photosynthesis and night time respiration were evident. Salinity again decreased markedly around 21:00.

pCO_2 remained below atmospheric levels, and the CO_2 flux was consistently negative, indicating net CO_2 uptake. The flux was strongly influenced by wind speed: when wind speed decreased at 18:00 and 21:00 on 19 May, the flux approached zero, whereas CO_2 uptake intensified at 13:00 on 20 May.

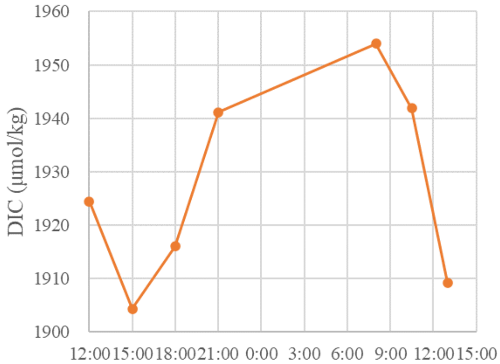
DIC (μmol/kg)
1960
1950
1940
1930
1920
1910
1900
12:00 15:00 18:00 21:00 0:00 3:00 6:00 9:00 12:00 15:00

(a)

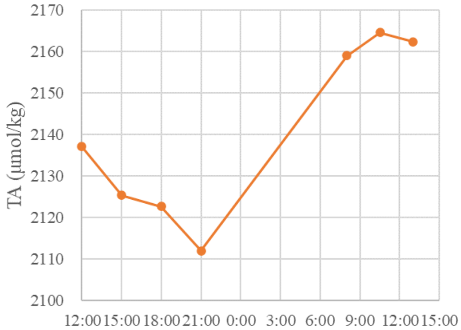
TA (μmol/kg)
2170
2160
2150
2140
2130
2120
2110
2100
12:00 15:00 18:00 21:00 0:00 3:00 6:00 9:00 12:00 15:00

(b)

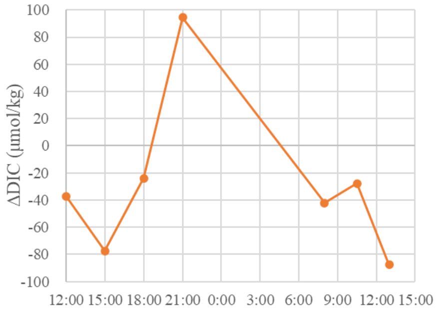
ΔDIC (μmol/kg)
100
80
60
40
20
0
-20
-40
-60
-80
-100
12:00 15:00 18:00 21:00 0:00 3:00 6:00 9:00 12:00 15:00

(c)

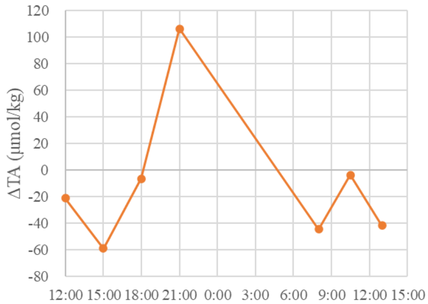
ΔTA (μmol/kg)
120
100
80
60
40
20
0
-20
-40
-60
-80
12:00 15:00 18:00 21:00 0:00 3:00 6:00 9:00 12:00 15:00

(d)

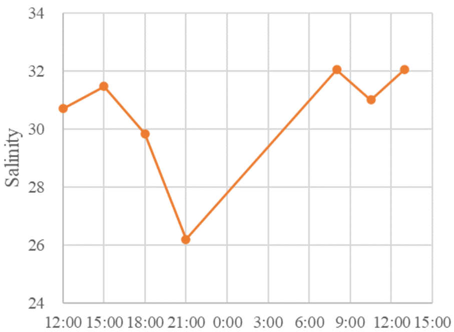
Salinity
34
32
30
28
26
24
12:00 15:00 18:00 21:00 0:00 3:00 6:00 9:00 12:00 15:00

(e)

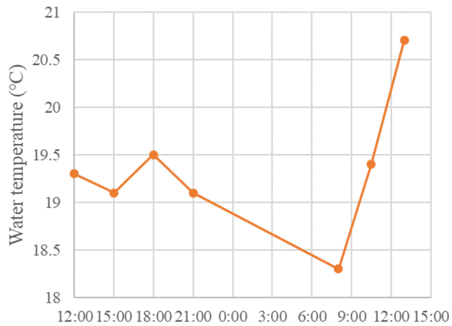
Water temperature (°C)
21
20.5
20
19.5
19
18.5
18
12:00 15:00 18:00 21:00 0:00 3:00 6:00 9:00 12:00 15:00

(f)

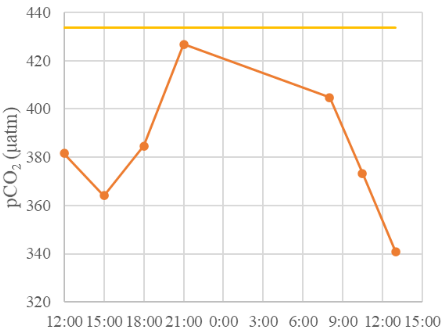
pCO2 (μatm)
440
420
400
380
360
340
320
12:00 15:00 18:00 21:00 0:00 3:00 6:00 9:00 12:00 15:00

(g)

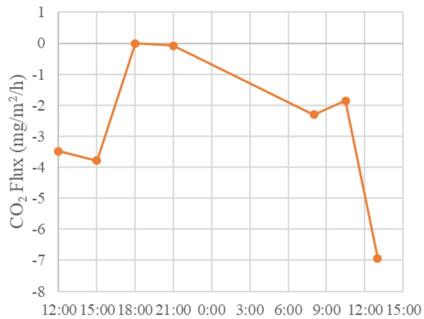
CO2 Flux (mg/m2/h)
1
0
-1
-2
-3
-4
-5
-6
-7
-8
12:00 15:00 18:00 21:00 0:00 3:00 6:00 9:00 12:00 15:00

(h)

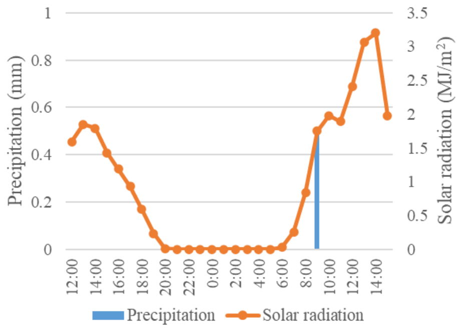

(i) (at St Minamata and St. Kumamoto)

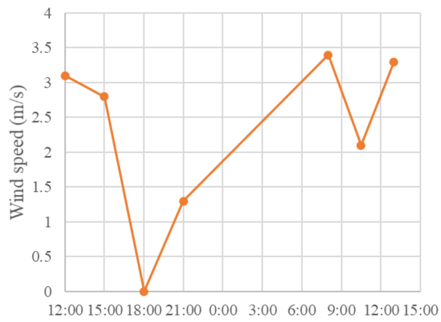

(j)

St. B

Fig. 3.6 Time-series of observed and calculated data on May 19-20, 2025: DIC (a), TA (b), ΔDIC (c), ΔTA (d), salinity (e), water temperature (f), pCO_2 (g), CO_2 flux (h), precipitation at St. Minamata and solar radiation St. Kumamoto (i), and wind speed (j). (The yellow line indicates atmospheric pCO_2.)

Across all observation years, ΔDIC consistently exhibited pronounced negative values during daytime, indicating that this eelgrass meadow functions as a strong carbon sink. In 2024 and 2025, clear-sky conditions and sufficient solar radiation enhanced photosynthetic carbon uptake, resulting in larger absolute values of ΔDIC and CO_2 flux. In contrast, during the rainy or cloudy conditions of 2021 and 2022, reduced solar radiation suppressed photosynthesis, leading to smaller absolute values of ΔDIC and the flux. These findings suggest that the blue carbon sequestration capacity of this area is highly sensitive to variations in solar radiation.

Although nighttime observations (21:00 to 06:00) were not conducted in 2024 and 2025 and the dataset is therefore incomplete, available results indicate that CO_2 did not shift to net emission at night and that net uptake into seawater was maintained. Enhanced air–sea gas exchange driven by wind speed at the sea surface likely contributed to this sustained absorption, suggesting that this eelgrass meadow functions as a stable CO_2 sink under diverse environmental conditions.

In general, ΔTA exhibited patterns similar to those of ΔDIC. Because the calculated DIC and TA values used to derive ΔDIC and ΔTA strongly depend on salinity, salinity variability plays a critical role in their apparent fluctuations. Although interannual differences were observed, significant decreases in salinity around 15:00 and 21:00 were recorded in multiple years. To clarify whether these fluctuations are driven by anthropogenic influences or natural processes, further investigation of the surrounding hydrological and geographical conditions, together with longer-term observations, is required.

3.2 Comparison of weather, day and night, and tides

All six observation campaigns were classified into two weather categories ("sunny" and "rainy/cloudy" condition), and a comparative analysis was conducted using eight subcategories defined by "day/night" and "tidal level (low/high water)." Tidal data were obtained from the nearest St. Minamata. Here, tidal levels higher than the mean tide level during each observation period were defined as high water, and those lower than the mean were defined as low water.

3.2.1 ΔDIC

Figure 3.7 presents a comparison of ΔDIC under different weather and tidal condition. Under clear-sky conditions, the contrast between daytime and nighttime values was pronounced, whereas differences associated with tidal level were relatively small. Among the four subcategories, the lowest mean value was observed under "Day/Low-tide" condition, reaching - 68.78 μmol/kg. This likely reflects the combined effect of reduced water depth at low tide and strong solar radiation, which together enhance the photosynthetic efficiency of eelgrass per unit water volume.

In contrast, under rainy or cloudy conditions, the distinction between daytime and nighttime values became much less evident. The magnitude of negative ΔDIC during daytime was also reduced, indicating that carbon uptake through photosynthesis is strongly constrained by meteorological conditions.

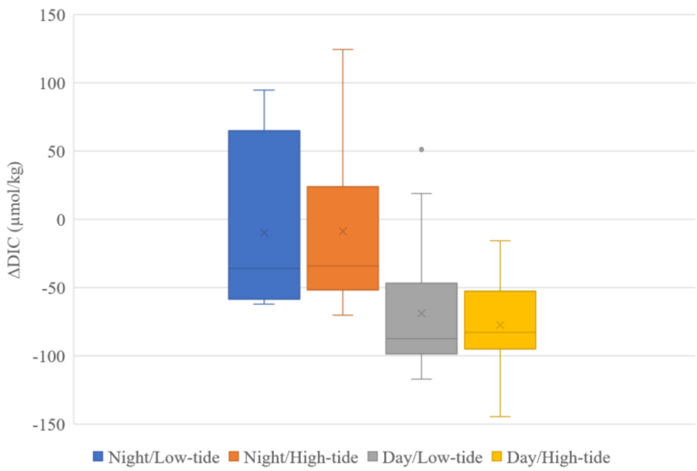

(a)

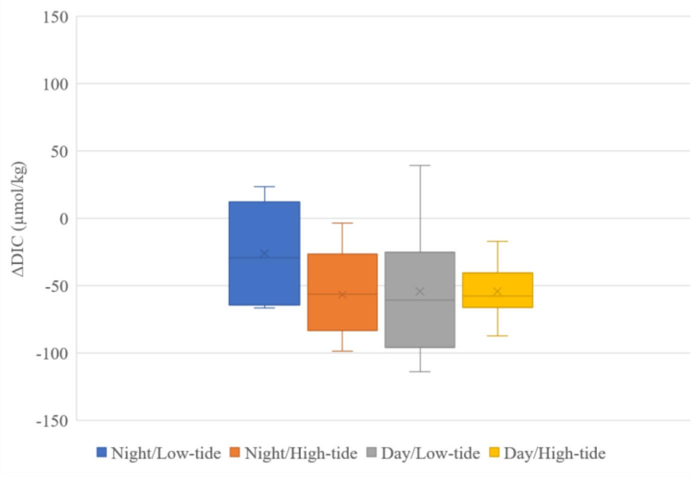

(b)

Fig. 3.7 Comparison of ΔDIC by weather, diurnal, and tidal conditions: Sunny condition (a) and Rainy and Cloudy condition (b).

3.2.2 pCO_2

Figure 3.8 presents a comparison of pCO_2 under different weather conditions and tidal conditions. Overall, the deviation from atmospheric CO_2 was greater under clear-sky conditions than under cloudy conditions. In particular, under "Day/Low-tide" condition during clear weather, the lower whisker of pCO_2 reached approximately 260 μatm, indicating the largest air–sea pCO_2 gradient.

Conversely, under the "Night/Low-tide" condition in cloudy/rainy weather, pCO_2 values were distinctly higher than those in the other three subcategories. This likely reflects the accumulation of CO_2 released through respiration in the surface layer. Under cloudy conditions, no substantial differences were observed among the subcategories, further demonstrating the strong influence of weather on pCO_2. Nevertheless, most pCO_2 values remained below the atmospheric levels, indicating persistent net CO_2 uptake.

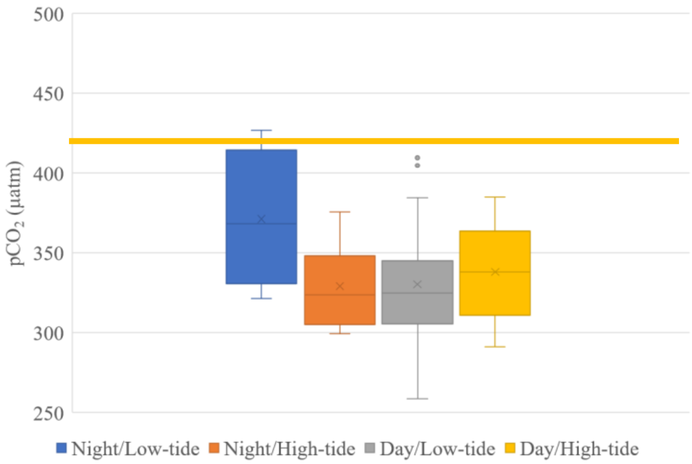

(a)

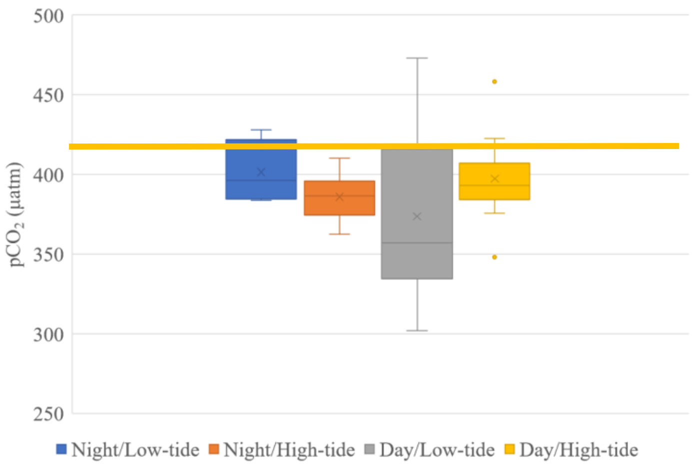

(b)

Fig. 3.8 Comparison of pCO_2 by weather, diurnal, and tidal conditions: Sunny condition (a) and Rainy and Cloudy condition (b).

3.2.3 Air-sea CO_2 flux

Figure 3.9 shows a comparison of CO_2 flux under different weather and tidal conditions. Similar to pCO_2, CO_2 flux exhibited marked variability depending on weather conditions. Under cloudy conditions, flux values were generally close to zero across all subcategories. In contrast, under clear-sky conditions, flux values were strongly negative, indicating enhanced CO_2 uptake. Among these, "Day/High-tide" category showed a relatively small interquartile range in the box plot, suggesting comparatively stable flux under this condition.

Figure 3.10 presents the mean flux values for each subcategory, and **Table 3.1** summarizes these values together with the percentage reduction in flux from clear to rainy/cloudy conditions. Under both weather conditions, flux values were negative, indicating net CO_2 absorption. The largest absolute mean flux was observed under "Night/High-tide", likely reflecting the influence of wind speed during the observations.

The reduction rates associated with weather conditions were substantial. For example, under the "Day/Low-tide" condition, the flux decreased from −4.74 mg m^{-2} h^{-1} in clear weather to −1.06 mg m^{-2} h^{-1} in rainy/cloudy weather, representing a 77.7% reduction. The highest reduction rate (98.0%) was observed under "Night/Low-tide", highlighting the strong sensitivity of air-sea CO_2 exchange to meteorological conditions.

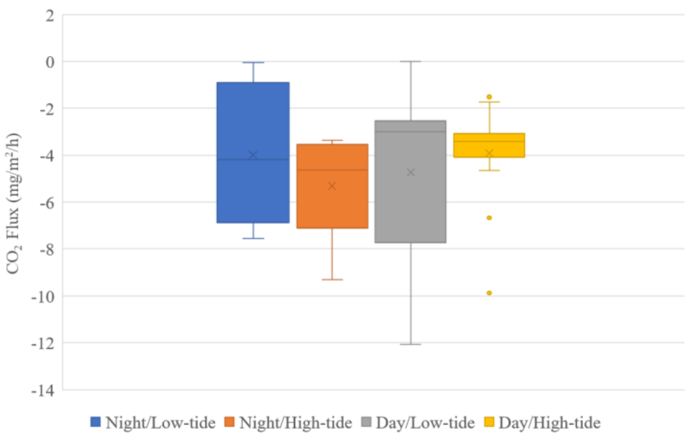

(a)

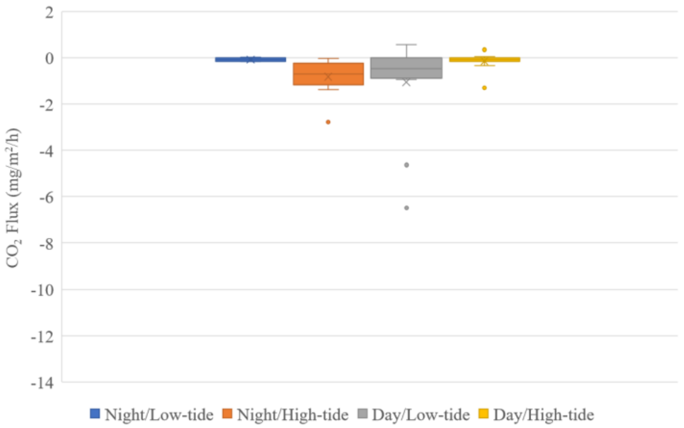

(b)

Fig. 3.9 Comparison of CO_2 flux by weather, diurnal, and tidal conditions: Sunny condition (a) and Rainy and Cloudy condition (b).

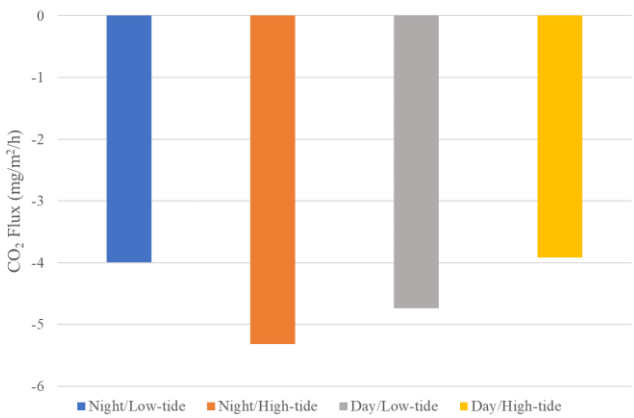

(a)

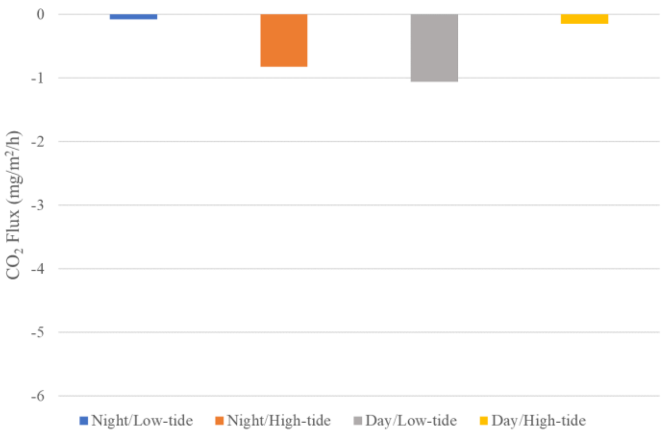

(b)

Fig. 3.10 Comparison of mean flux values under each condition: Sunny condition (a) and Rainy and Cloudy condition (b).

Table 3.1 Mean CO_2 flux under each condition and reduction rate

	Night/low	Night/High	Day/low	Day/High
Sunny	-3.99	-5.32	-4.74	-3.92
Rainy/Cloudy	-0.0783	-0.827	-1.06	-0.145
Reduction rate (%)	98.0	84.4	77.7	96.3

3.3 Analysis of the Influence of Various Factors on pCO_2

3.3.1 Simple Regression Analysis

To identify the factors controlling pCO_2 variability, regression analyses were conducted using pCO_2, water temperature, salinity, TA, DIC, ΔTA, ΔDIC, and CO_2 flux as variables. The results of the simple linear regression analyses are shown in **Fig 3.11**.

The simple regression analysis revealed a strong positive correlation between pCO_2 and DIC (R = 0.68), and a weak positive correlation between pCO_2 and ΔDIC (R = 0.20). In addition, an extremely strong correlation was found between ΔDIC and ΔTA (R = 0.86). These results indicate the presence of strong collinearity between ΔDIC and ΔTA. Therefore, to avoid a reduction in estimation accuracy due to multicollinearity, ΔTA was excluded from the explanatory variables in the multiple regression analysis.

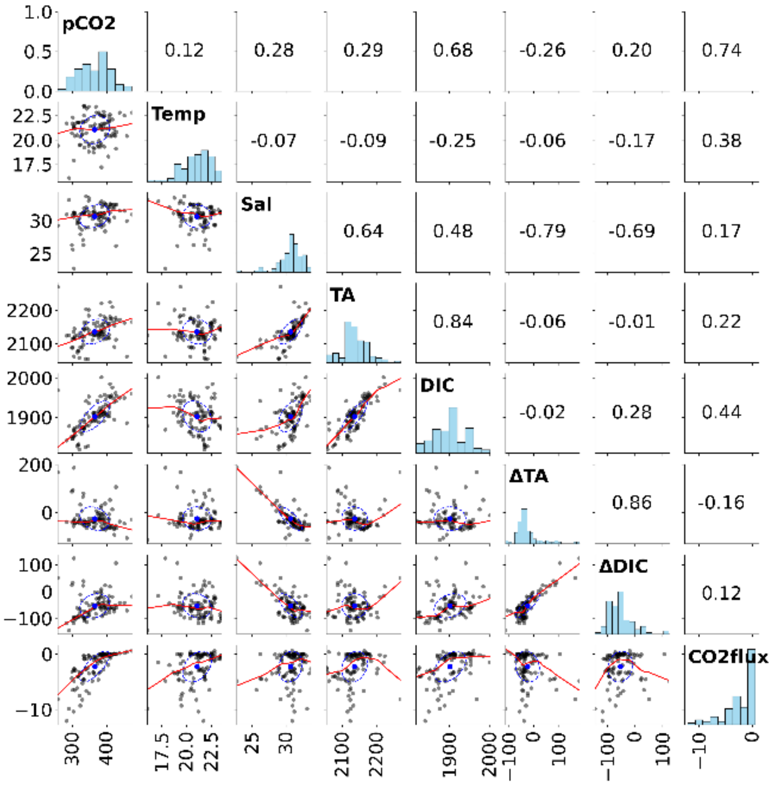

Fig. 3.11 Result of simple regression analysis

Note 1) The upper triangular matrix shows the Pearson correlation coefficients, the lower triangular matrix displays scatter plots (including a smoothing curve, a 95% confidence ellipse and its centroid), and the diagonal elements present histograms.

Note 2) The units of each variable are as follows: seawater pCO_2 (μatm), water temperature (°C), salinity (PSU), TA (μmol/kg), DIC (μmol/kg), ΔDIC (μmol/kg), ΔTA (μmol/kg), and CO_2 flux (μatm).

3.3.2 Multiple Regression Analysis

A multiple regression analysis was then performed with pCO_2 as the dependent variable and water temperature, salinity, ΔDIC, wind speed, tidal variation, precipitation, air temperature, and solar radiation as explanatory variables (see **Table 3.2** to **Table 3.4**). The coefficient of determination was $R^2 = 0.749$, indicating that the model explained approximately 75% of the variability in pCO_2. The overall regression model was highly significant ($F = 37.98$, $p = 8.29 \times 10^{-26}$), indicating that the model explains a statistically significant proportion of the variance in pCO_2. Comparison of the standardized regression coefficients (β) showed that ΔDIC had the largest contribution to pCO_2 dynamics (β = 1.02), followed by salinity (β = 0.93). Conversely, Tidal variation ($p = 0.387$) and air temperature ($p = 0.897$) were not statistically significant.

Table 3.2 Regression statistics

Multiple R	0.887
R Square R^2	0.770
Adjusted R Square	0.749
Standard Error	0.503
Observations	100

Table 3.3 Analysis of variance

	Degrees of Freedom	Sum of Squares	Mean Square	F	Significance F
Regression	8	76.952	9.619	37.979	8.29E-26
Residual	91	23.048	0.253		
Total	99	100			

Table 3.4 Estimated regression coefficients

	Coefficient	Standard Error	t Stat	P-value
Intercept	-4.3E-15	0.050	-8.5E-14	1.000
Water Temperature	0.302	0.063	4.797	6.28E-06
Salinity	0.933	0.081	11.539	1.65E-19
ΔDIC	1.020	0.080	12.677	8.18E-22
Wind Speed	-0.147	0.058	-2.530	1.31E-02
Tidal Variation	0.046	0.053	0.869	3.87E-01
Precipitation	0.316	0.055	5.766	1.10E-07
Air Temperature	0.008	0.063	0.130	8.97E-01
Total Solar Radiation	-0.368	0.053	-6.885	7.25E-10

3.4 Variations and Model Reproducibility

3.4.1 pCO_2

Figure 3.12 presents the time series of observed and simulated pCO_2 in 2022 and 2023, respectively. “New” refers to the model improved in this study, whereas “Old” indicates the existing model. These calculated values were compared with the observed values at St. B, which was selected as a representitive site.

In 2022, two distinct peaks were observed in pCO_2. These peaks were generally reproduced by the new model between 00:00 and 12:00. However, the model failed to capture the observed variations during other periods (e.g., 18:00 and 21:00 on 10 June, and 15:00 and 18:00 on 11 June). The existing model was unable to reproduce these fluctuations at all,, indicaating that the improved model provides a prtial enhancement in performance.

In contrast, for 2023, the new model failed to reproduce the pronoounced peaks observed at 04:00 and 07:00 on 17 May and instead showed fluctuations in the opposite direction. Nevertheless, the relatively lower pCO_2 values during other time periods were reproduced reasonably well. The existing model failed to reproduce the peaks, and showed almost no temporal variability.

Figure 3.13 compares observed and simulated pCO_2 values in both years. Some data points lie close to the 1:1 line (the orange line), whereas others deviate substantially, indicating that the model performance varies depending on the time periods. Overall, reproducibility of pCO_2 can be considered moderate.

As described in Section 2.6, pCO_2 is not directly simulated within the model but is calculated based on the chemical equilibrium relationships in the carbon system. Therefore, the accuracy of simulated pCO_2 strongly depends on the accuracy of four key parameters; salinity, water temperature, TA, and DIC. In other words, further improvements in the simulation of these four variables are necessary to enhance the model’s ability to reproduce pCO_2 dynamics.

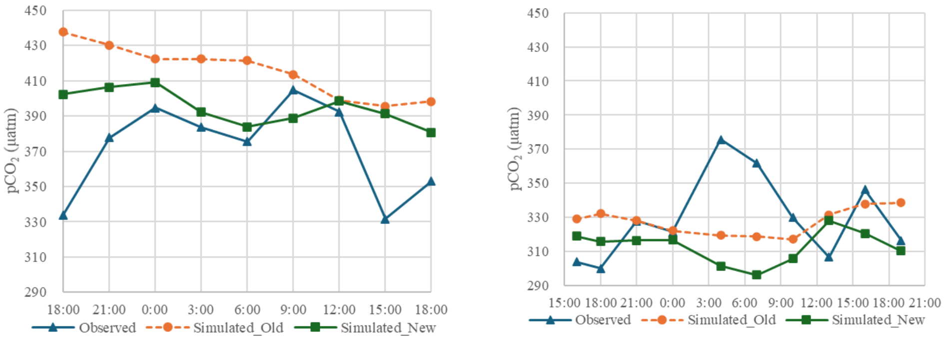

Fig. 3.12 Time-series of observed vs. simulated pCO_2 for 2022 (left) and 2023 (right)

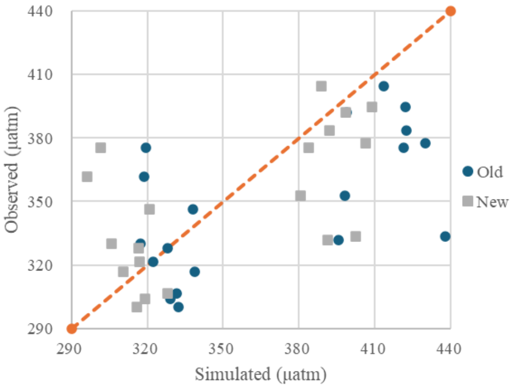

Fig. 3.13 Comparison of observed and simulated pCO_2 in 2022 and 2023

3.4.2 Water temperature

Figure 3.14 presents the time series of observed and simulated water temperature in 2022 and 2023, respectively. Water temperature is calculated directly within the Flow Model, therfore no comparison between the new model and old model is provided for this variable.

In 2022, the observed water temperature began to decrease at 00:00 on 11 June, and increased after 06:00 on 11 June. In contrast, the simulated temperature decreased continuously throughout the period. Although the model generally captured the overall decreasing trend, it failed to reproduce the observed variability.

In 2023, the observed temperature showed a similar pattern to that in 2022, decreasing during the nighttime and beginning to rise at around 07:00 on 17 May, reaching a minimum of less than 19°C at that time. The simulated temperature in 2023 reproduced the temporal trend more accurately than in 2022, as it showed both decreasing and increasing phases during the observation period. The mean differences of between observed and simulated temperature were 3.89 °C in 2022 and 2.95 °C in 2023. The model underestimates water temperature in both years.

Figure 3.15 compares between observed and simulated water temperature values. While the model reproduces the general trend reasonably well, the scatter plot shows that all data points deviate considerably from the 1:1 line, indicating limited quantitative accuracy.

To improve model performance with respect to water temperature, it may be necessary to recalibrate parameters related to heat flux calculations. As described in Section 2.7.4, the Murakami model was adopted in the Flow Model. Parameters such as sky cloudiness, Secchi depth, and the Dalton number can be adjusted within Delft3D-FLOW to improve simulation accuracy.

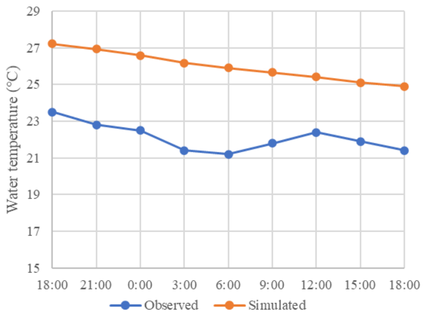

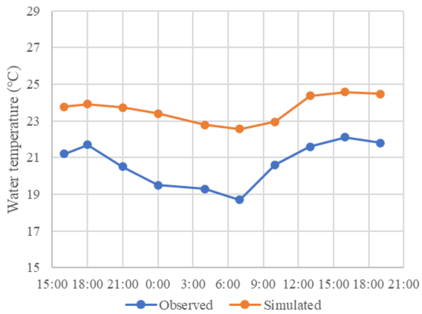

Fig. 3.14 Time-series of observed vs. simulated water temperature for 2022 (left) and 2023 (right)

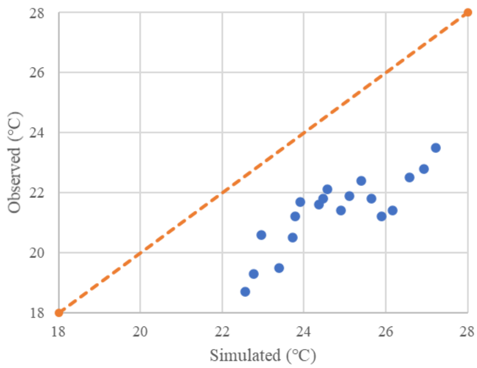

Fig. 3.15 Comparison of observed and simulated water temperature in 2022 and 2023

3.4.3 Salinity

Figure 3.16 presents the time series of observed and simulated salinity in 2022 and 2023, respectively. Salinity is also calculated within the Flow Model, therefore the results of new model is same as the existing model.

In 2022, simulated salinity fluctuated slightly between 31 and 32, whereas in 2023 it ranged between 30 and 31. In contrast, the observed salinity in both years exhibited substantial temporal variability, with maximum fluctuations of approximately 4 units. The simulated salinity remained nearly constant throughout the observation periods and did not reproduce the observed variability. **Figure 3.17** further illustrates this discrepancy, showing that the simulated values cluster within a narrow range, while the observed values are widely scattered.

In general, salinity in semi-enclosed coastal areas is expected to remain relatively stable unless influenced by significant freshwater input, such as heavy rainfall or river discharge. Although 2022 was characterized by cloudy and rainy conditions and 2023 by clear weather, the magnitude and timing of the observed salinity decreases do not appear to be directly explained by meteorological conditions alone. Furthermore, as described in Section 2.2, the observation site is located within a port protected by a breakwater, suggesting that direct riverine influence may be limited.

Interestingly, salinity decreases were observed at similar times in both years (e.g., around 21:00 and approximately 15:00). This recurring pattern suggests the possibility of localized influences. While natural processes cannot be ruled out, potential anthropogenic factors may also contribute to these fluctuations. For example, intermittent freshwater discharge from nearby industrial or fishery-related facilities could affect salinity within the port. However, due to the limited number of observation campaigns, it is not possible to determine the exact cause. As mentioned in Section 3.1, further field investigations and longer-term monitoring are required to clarify the mechanisms responsible for these variations.

In addition, numerical models generally reproduce conditions in the central part of the computational domain more accurately than those near open or land boundaries. Model accuracy near boundaries strongly depends on grid resolution and boundary conditions. Because the study area is located in a coastal region close to model boundaries, it may be challenging to accurately simulate localized salinity variations. Refinement of grid cell size and recalibration of salinity-related boundary and mixing parameters may therefore improve model performance.

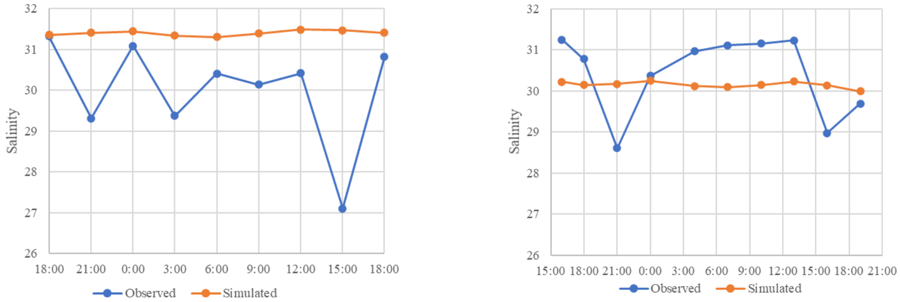

Fig. 3.16 Time-series of observed vs. simulated salinity for 2022 (left) and 2023 (right)

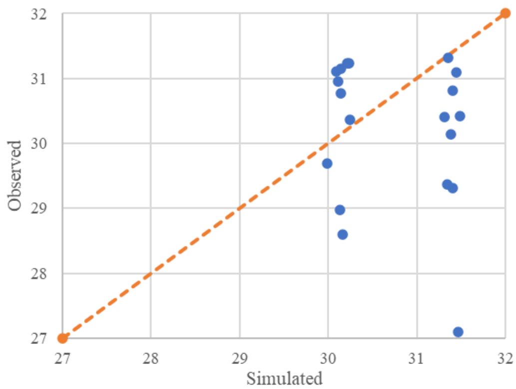

Fig. 3.17 Comparison of observed and simulated salinity in 2022 and 2023

3.4.4 Total alkalinity

Figure 3.18 presents the time series of observed and simulated TA in 2022 and 2023, respectively.

In 2022, the simulated TA exhibited temporal fluctuations similar to those observed, although noticeable differences remained between the two datasets. In contrast, in 2023, between 00:00 and 10:00 on 17 May, the simulated values fluctuated in the opposite direction to the observed values. Moreover, the discrepancy between observed and simulated TA was larger in 2023 than in 2022. The mean differences were 57.8 μmol/kg in 2022 and 110 μmol/kg in 2023, indicating substantially lower model performance in 2023.

Figure 3.19 compares observed and simulated TA values. Although the overall trend is reproduced to some extent, clear deviations are present, and the model generally underestimates TA.

As described in Section 2.6, TA is calculated within LTLE Model, meaning that its accuracy is influenced by the simulation results of the Flow Model.

Therefore, errors in salinity and water temperature in the FLOW Model can propagate into the LTLE Model calculations and affect TA reproducibility.

Biological processes, including seagrass and phytoplankton activity, may also influence TA through nutrient-related processes. However, these effects are relatively indirect and generally smaller than their impact on DIC, since photosynthesis and respiration directly alter DIC through CO_2 uptake and release.

Accordingly, improving the hydrodynamic accuracy of the Flow Model is expected to enhance TA reproducibility. In addition, recalibration of biological parameters related to seagrass processes may further improve model performance.

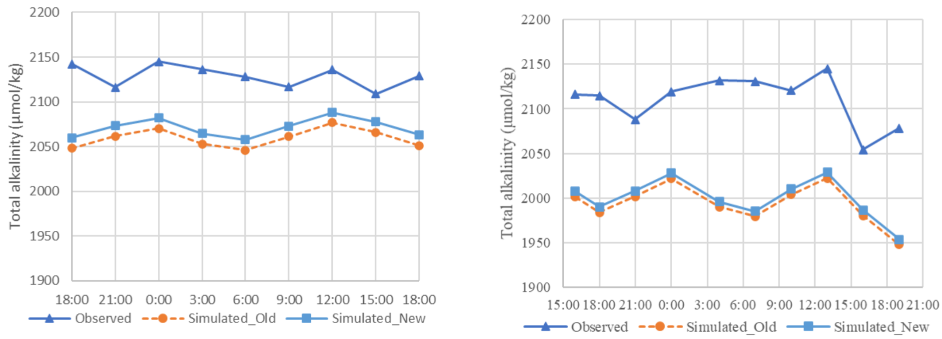

Fig. 3.18 Time-series of observed vs. simulated total alkalinity for 2022 (left) and 2023 (right)

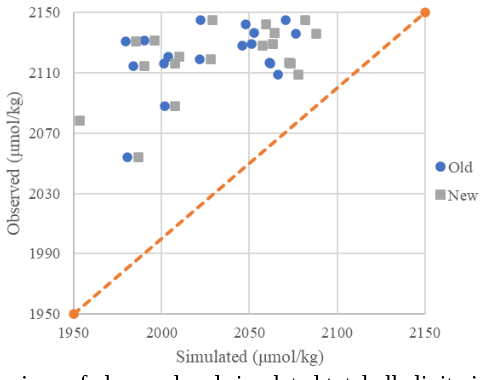

Fig. 3.19 Comparison of observed and simulated total alkalinity in 2022 and 2023

3.4.5 Dissolved inorganic carbon

Figure 3.20 shows the time series of observed and simulated DIC in 2022 and 2023, respectively.

Similar to TA, the simulated DIC in 2022 generally captured the temporal trend of the observations, although discrepancies remained. In contrast, in 2023, the model failed to reproduce the observed variability between 00:00 and 10:00 on 11 June. The mean differences between observed and simulated DIC were 71 μmol/kg in 2022 and 119 μmol/kg in 2023, indicating reduced model performance in 2023.

Visually, the difference between the new and existing models in terms of DIC appears minor. However, the resulting differences in calculated pCO_2 between the two models are substantial as shown before. This reflects the nonlinear and complex nature of carbonate system equilibrium equations, in which small variations in DIC (and TA) can lead to amplified changes in pCO_2. Because pCO_2 is derived from multiple interacting parameters through nonlinear chemical relationships, it is difficult to isolate which specific parameter adjustments most strongly influence its variability.

Figure 3.21 compares observed and simulated DIC values. Although the general trend is reproduced reasonably well, noticeable deviations remain between observations and simulations.

Detailed numerical results for pCO_2, water temperature, salinity, TA, and DIC in 2022 and 2023 are provided in **Table B1** to **Table B3**, Appendix.

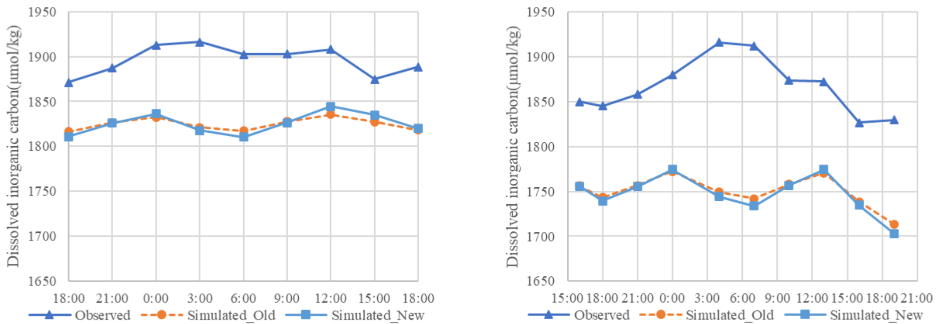

Fig. 3.20 Time-series of observed vs. simulated dissolved inorganic carbon for 2022 (left) and 2023 (right)

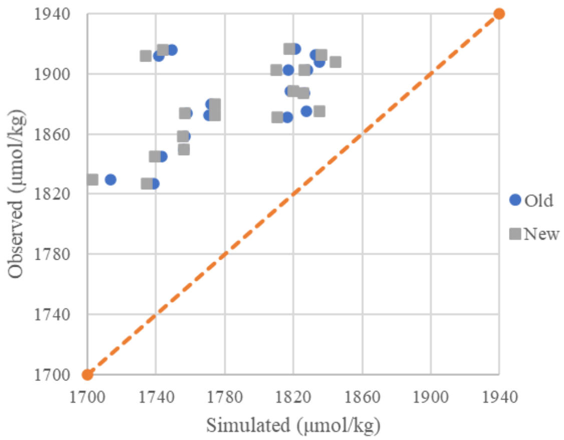

Fig. 3.21 Comparison of observed and simulated dissolve inorganic carbon in 2022 and 2023

3.5 Comprehensive Statistical Evaluation

Table 3.5 summarizes the correlation coefficient (R) and the Root Mean Square Percentage Error (RMSPE) for four key parameters (water temperature, salinity, TA, and DIC) as well as pCO_2.

The correlation coefficient (R) represents how well the model reproduces the temporal trend of observations and ranges from -1 to 1. Values closer to 1 indicate strong positive agreement between simulated and observed variations, whereas values near 0 indicate poor reproduction of the temporal pattern. However, a limitation of R is that it does not account for systematic bias between simulations and observations. For example, even if simulated water temperature consistently differs from observations by 20 ^{o}C, R may still approach 1 provided that the temporal fluctuations are identical.

For this reason, RMSPE was also calculated. RMSPE quantifies the magnitude of deviation between predicted and observed values as a percentage, enabling comparison among parameters with different units and scales.

According to **Table 3.5**, water temperature exhibits the highest R among the five variables, indicating that its temporal trend is reproduced relatively well. However, its RMSPE is comparatively large, reflecting a substantial systematic bias. As discussed earlier, the model tends to overestimate water temperature; therefore, recalibration is necessary to reduce this bias.

In contrast, salinity shows a very low R despite a moderate RMSPE. This indicates that although the overall magnitude of error is not large, the model fails to reproduce temporal variability adequately. Since both water temperature and salinity are calculated within the Flow Model, improving the hydrodynamic model is essential for enhancing their reproducibility.

For TA, DIC, and pCO_2, performance of the new model can be compared with that of the existing model. For TA, overall performance remains similar between models: although R slightly decreases, RMSPE shows marginal improvement. For DIC, R improves in the new model, whereas RMSPE becomes slightly worse.

In contrast, pCO_2 shows noticeable improvement in the new model, particularly in terms of R, which becomes substantially closer to 1. Nevertheless, RMSPE remains relatively large, second only to that of water temperature. As previously discussed, the reproducibility of pCO_2 strongly depends on the accuracy of water temperature, salinity, TA, and DIC. Therefore, further improvements in these four parameters are essential to enhance overall pCO_2 simulation performance.

Table 3.5 Correlation coefficient *R* and *RMSPE*

	Correlation coefficient *R*	*RMSPE* (%)
Water temperature	0.840 ($p < 0.05$)	16.4
Salinity	0.187 ($p > 0.05$)	5.13
TA (Old)	0.551 ($p < 0.05$)	4.68
TA (New)	0.545 (p < 0.05)	4.33
DIC (Old)	0.534 (p < 0.05)	5.31
DIC (New)	0.589 ($p < 0.05$)	5.43
pCO_2 (Old)	0.615 ($p < 0.05$)	17.3
pCO_2 (New)	0.717 ($p < 0.05$)	14.3

4. Conclusions

In this study, the factors controlling pCO_2 dynamics were investigated using multi-year observational data. In addition, the existing LTLE model was enhanced by incorporating processes related to submerged macrophytes (seagrass) in order to better simulate pCO_2 dynamics.

The key findings based on the analysis of observation data and the improved model are summarized as follows:

- pCO_2 reached its minimum values under clear-sky, daytime, and low-tide conditions, when photosynthetic activity was maximized, resulting in substantial CO_2 uptake.
- Under rainy or cloudy conditions, reduced solar radiation suppressed photosynthesis, and CO_2 uptake decreased to approximately one quarter of that observed under clear-sky conditions, corresponding to a reduction rate of at least 77.7 %.
- Multiple regression analysis indicated that ΔDIC and salinity had the largest regression coefficients with respect to pCO_2, followed by water temperature and precipitation.
- Incorporation of seagrass processes improved the simulation of pCO_2, particularly during specific time periods in both 2022 and 2023. However, temporal variability of pCO_2 was not fully reproduced by the improved model.
- The reproducibility of salinity was considerably lower than that of the other parameters, with little simulated temporal variability, whereas water temperature, TA, and DIC showed moderate reproducibility but exhibited systematic or persistent biases.
- Model performance in coastal areas was lower than that reported in previous studies conducted in more central regions of the computational domain. Even fundamental physical variables such as water temperature and salinity did not show sufficient reproducibility in this coastal setting.

In summary, the present model is not yet sufficient to fully reproduce pCO_2 dynamics in coastal areas. Further field observations and continued model refinement are required. In particular, improvements in the simulation of water temperature and salinity within the Flow Model are essential. Enhancing spatial resolution and improving boundary condition specifications may increase model accuracy in coastal regions. Furthermore, to better represent seagrass processes, respiration should be explicitly separated from phytoplankton respiration, and more accurate parameterization of seagrass photosynthesis is necessary.

References

Arakawa, H., Kanda, Y. & Ishihara, T. (2007). "Proposal of a method for estimating offshore wind speed using a three-dimensional wind field model". *Journal of Japan Society of Civil Engineers, Ser. B2 (Coastal Engineering)*, 54(2), pp. I_131-I_135. https://doi.org/10.2208/proce1989.54.131 (in Japanese)

Arina, N., Hidayah, N., Hazrin-Chong, N. H. & Rozaimi, M. (2023). "Algal contribution to organic carbon sequestration and its signatures in a tropical seagrass meadow". *Deep Sea Research Part II: Topical Studies in Oceanography*, 210. https://doi.org/10.1016/j.dsr2.2023.105307

Blauw, A.N., Los, H.F.J., Bokhorst, M., & Erftemeijer, P.L.A. (2009). "GEM: A generic ecological model for estuaries and coastal waters". *Hydrobiologia*, 618(1), pp.175-198. https://doi.org/10.1007/s10750-008-9575-x

Borges, A. V., Vanderborght, J. P., Schiettecatte, L. S., Gazeau, F., Ferron-Smith, S., Delille, B. & Frankignoulle, M. (20224). "Variability of the gas transfer velocity of CO_2 in a macrotidal estuary (the Scheldt)". *Estuaries and Coasts*, 27, pp.593-603. https://doi.org/10.1007/BF02907647

Borges, A. V., Delille, B. & Frankignoulle, M. (2005). "Budgeting sinks and sources of CO_2 in the coastal ocean: Diversity of ecosystems counts". *Geophysical Research Letters*, 32(14). https://doi.org/10.1029/2005GL023053

Chambers, J. Q., Higuchi, N., Tribuzy, E. S. & Trumbore, S. E. (2001). "Carbon sink for a century". *Nature*, 410, pp.429. https://www.nature.com/articles/35068624

Deltares (2018a). Delft3D-FLOW: Simulation of multi-dimensional hydrodynamic flows and transport phenomena, including sediments, User Manual. Delft, The Netherlands: Deltares.

Deltares (2018b). D-Water Quality Processes Library Description: Detailed description of Processes, Technical Reference Manual. Delft, The Netherlands: Deltares.

Deltares (2018c). D-Water Quality Processes Library Tables: Technical Reference Manual. Delft, The Netherlands: Deltares.

Dickson, A.G. (1981). “An exact definition of total alkalinity and a procedure for the estimation of alkalinity and total inorganic carbon from titration data”. *Deep Sea Research Part A. Oceanographic Research Papers*, 28, pp.609-623. http://dx.doi.org/10.1016/0198-0149(81)90121-7

Duarte, C. M., Marba, N., Gacia, E., Fourqurean, J. W., Beggins, J., Barron, C. & Apostolaki, E. T. (2010). “Seagrass community metabolism: Assessing the carbon sink capacity of seagrass meadows”. *Global Biogeochemical Cycles*, 24(4). https://doi.org/10.1029/2010GB003793

Gruber, N., Bakker, D.C.E., DeVries, T., Gregor, L., Hauck, J., Landschutzer, P., McKinley, G. A. & Muller, J. D. (2023). “Trends and variability in the ocean carbon sink”. *Nature Review Earth & Environment*, 4, pp.119–134. https://doi.org/10.1038/s43017-022-00381-x

Gurel, M., Tanik, A., Gonec, E., & Russo, R.C. (2005). “Biogeochemical Cycles”, in: Wolflin, J.P. & Gonenc I.E. (eds.) *Coastal Lagoons*. Boca Raton: CRC Press.

Ishizaki, H. & Mitsuta, Y. (1962). “On the spatial extent of gusts and gust factor during strong winds”. *Annuals of the Disaster Prevention Research Institute, Kyoto University*, No. 5A, pp. 135–138. (in Japanese)

Japan Road Association. (2007). *Manual for Wind-Resistant Design of Highway Bridges*. pp295. (in Japanese)

Komatsu, T., Sagawa, R. & Mikami, A. (2006). “Distribution and Ecological Roles of Macroalgal Beds in Tidal Flat Ecosystems”. *Global Environment*, 11(2), pp207-213. (in Japanese)

Komori, H., Xiong, B., Saito, N., Hao, L., Chi, B., Yano, S., Komai, K. & Nakayama, K. (2021). “Numerical modelling of CO_2 dynamics in seawater considering the effects of freshwater inflow in the Yatsushiro Sea”. *Journal of Japan Society of Civil Engineers, Ser. B2 (Coastal Engineering)*, 77(2), pp.I_847-I_852. (in Japanese)

Krause-Jensen, D. & Duarte, C. M. (2016). “Substantial role of macroalgae in marine carbon sequestration”. *Nature Geoscience*, 9, pp.737-742. https://doi.org/10.1038/ngeo2790

Kristensen, E. & Holmer, M. (2001). “Decomposition of plant materials in marine sediment exposed to different electron acceptors (O_2, NO_3^-, and SO_4^{2-}), with emphasis on substrate origin, degradation kinetics, and the role of bioturbation”. *Geochimica et Cosmochimica Acta*, 65(3), pp.419-433. https://doi.org/10.1016/S0016-7037(00)00532-9

Nellemann, C., Corcoran, E., Duarte, C., Valdés, L., Young, C. D., Fonseca, L. & Grimsditch, G. “Blue Carbon, The Role of Healthy Oceans in Binding Carbon”. *United Nations Environmental Programme, GRID-Arendal.*

Nishimura, N., Watanabe, K., Kishida, T., Iwata, T. & Otaki, E. (1998). “Variation of partial pressure of carbon dioxide (pCO_2) in river water”. *Environmental Science*, 11(3), pp.297-304. https://doi.org/10.11353/sesj1988.11.297 (in Japanese)

Mcleod, E., Chmura, G. L., Bouillon, S. B., Salm, R., Bjork, M., Duarte, C. M., Lovelock, C. E., Schlesinger, W. H. & Silliman, B. R. (2011). “A blueprint for blue carbon: toward an improved understanding of the role of vegetated coastal habitats in sequestering CO_2”. *Frontiers in Ecology and the Environment*, 9(10), pp.552-560. https://doi.org/10.1890/110004

Ministry of the Environment, Japan (2008). “Seventh National Survey on the Natural Environment: Comprehensive Report on the Coastal Survey”. Available at: https://www.biodic.go.jp/kiso/34/34_higat.html#mainText (Accessed: 16 January 2021)

Ministry of the Environment, Japan (2021). “Results of the distribution survey of seagrass beds and tidal flats in the southern Ariake Sea area and the Yatsushiro Sea”.
Moritsch, M. M., Gallagher, A. J., Harris, S. D., Howe, W., Fu, C., Bervoets, T. & Duarte, C. M. (2025). “Carbon dynamics under loss and restoration scenarios in the world’s largest seagrass meadow”. *Scientific Reports*, 15. https://doi.org/10.1038/s41598-025-01993-1

Murakami, M., Oonishi, Y. & Kunishi, H. “A numerical simulation of the distribution of water temperature and salinity in the Seto Inland Sea”. *Journal of the Oceanographical Society of Japan*, 41, pp.213–224.

Press release, 15 January 2021. Available at: https://www.env.go.jp/press/108911.html?utm_source=chatgpt.com
(Accessed: 5 January 2021)

Qu, B., Song, J., Yuan, H., Li, X. & Li, N. (2018). "Carbon chemistry in the mainstream of the Kuroshio Current in eastern Taiwan and its transport of carbon into the East China Sea shelf". *Sustainability*, 10(3), 791. https://doi.org/10.3390/su10030791

Saito, N., Xiong, B., Komori, H., Yano, S., Nkayama, K., Komai, K. & Yajima, H. (2022). "Field investigation of CO_2 in seawater for understanding blue carbon dynamics in the Yatsushiro Sea". *Journal of Japan Society of Civil Engineers, Ser. B2 (Coastal Engineering)*, 76(2), pp.I_901-I_906. https://doi.org/10.2208/kaigan.76.2_I_901 (in Japanese)

Sohma, A., Nakai, M. Kubo, A. & Kuwae, T. (2018). "Seasonal variation and controlling factors of air–sea CO_2 flux in the estuarine area of Tokyo Bay: analysis using an ecosystem model incorporating carbonate chemistry". *Journal of Japan Society of Civil Engineers, Ser. B2 (Coastal Engineering)*, 74(2), pp.I_1267-I_1272. https://doi.org/10.2208/kaigan.74.I_1267 (in Japanese)

Suzuki, H. (1997). "Marine organisms and the carbon cycle". Tokyo: University of Tokyo Press. (in Japanese)

Tada, K., Tokoro, R., Watanabe, K. & Kuwae, T. (2013). "Factors influencing air–sea CO_2 flux in Lake Furen, Hokkaido". *Journal of Japan Society of Civil Engineers, Ser. B3 (Ocean Engineering)*, 69(2), pp.I_1252-I_1257. https://doi.org/10.2208/jscejoe.69.I_1252 (in Japanese)

Tada, K., Tokoro, R., Watanabe, K., Mogi, H. & Kuwae, T. (2014). "Continuous observation of air–sea CO_2 flux in a seagrass meadow". *Journal of Japan Society of Civil Engineers, Ser. B2 (Coastal Engineering)*, 70(2), pp.I_1191-I_1195. https://doi.org/10.2208/kaigan.70.I_1191 (in Japanese)

Tada, K., Nakayama, K. & Kuwae, T. (2018). "Development of a Seawater pCO_2 Model in Zostera marina Meadows". *Journal of Japan Society of Civil Engineers, Ser. B2 (Coastal Engineering)*, 74(2), pp.I_1237-I_1242. https://doi.org/10.2208/kaigan.74.I_1237 (in Japanese)

Tadokoro, S. & Yano, S. (2019). "Assessment of the effects of climate change–induced variations in temperature and river discharge on the formation and dissipation of hypoxic water masses in the Ariake Sea". *Journal of Japan Society of Civil Engineers, Ser. B2 (Coastal Engineering)*, 75(2), pp.I_1231-I_1236. https://doi.org/10.2208/kaigan.75.I_1231 (in Japanese)

Takahashi, T., Sutherland, S. C., Wanninkhof, R., Sweeney, C., Feely, R. A., Chipman, D. W., Hales, B., Friederich, G., Chavez, F., Sabine, C., Watson, A., Bakker, D. C. E., Schuster, U., Metzl, N., Yoshikawa-Inoue, H., Ishii, M., Midorikawa, T., Nojiri, Y., Kortzinger, A., Steinhoff, T., Hoppema, M., Olafsson, J., Arnarson, T. S., Tilbrook, B., Johannessen, T., Olsen, A., Bellerby, R., Wong, C. S., Delille, B., Bates, N. R. & de Baar, H. J. W. (2009). "Climatological mean and decadal change in surface ocean pCO_2, and net sea-air CO_2 flux over the global oceans". *Deep-Sea Research II*: *Topical Studies in Oceanography*, 56(8-10), pp.554-577. https://doi.org/10.1016/j.dsr2.2008.12.009

Tanaka, M., Inagaki, S. & Yamaki, K. (2002). "Tidal and three-dimensional hydrodynamic simulation in the Ariake Sea". *Proceedings of the Coastal Engineering, JSCE*, 49, pp.406-410. https://doi.org/10.2208/proce1989.49.406 (in Japanese)

Tokoro, T., Hosokawa, S., Miyoshi, E., Tada, K., Watanabe, K., Montani, S., Kayanne, H. & Kuwae, T. (2014). "Net uptake of atmospheric CO_2 by coastal submerged aquatic vegetation". *Global Change Biology*, 20(6), pp.1873-1884. https://doi.org/10.1111/gcb.12543

Tsunogai, S., Watanabe, S. & Sato, T. (2002). "Is there a 'continental shelf pump' for the absorption of atmospheric CO_2?". *Tellus, Series B: Chemical and Physical Meteorology*, 51(3), pp.701-712. https://doi.org/10.1034/j.1600-0889.1999.t01-2-00010.x

Wanninkhof, R. (1992). "Relationship between wind speed and gas exchange over the ocean". *Journal of Geophysical Research: Oceans*, 97(C5), pp.7373-7382. https://doi.org/10.1029/92JC00188

Ware, J. R., Smith, S. V. & Reaka-Kudla, M. L. (1992). "Coral reefs: sources or sinks of atmospheric CO_2". *Coral Reefs*, 11(3), pp.127-130. https://link.springer.com/article/10.1007/BF00255465

Weiss, R. F. (1974). "Carbon dioxide in water and seawater: the solubility of a non-ideal gas". *Marine Chemisty*, 2(3), pp.203-215. https://doi.org/10.1016/0304-4203(74)90015-2

Xiong, B., Yano, S., Komai, K., N., Saito, N., Komori, H., Chi, B., Hao, L. & Nakayama, K. (2022). "Interaction between seawater carbon dioxide dynamics and stratification in shallow coastal waters: A preliminary study based on a weekly validated three-dimensional ecological model". *Frontiers in Marine Science*, 9. https://doi.org/10.3389/fmars.2022.991802

Yamaguchi, S. & Hayami, Y. (2018). "Impact of Isahaya dike construction on DO concentration in the Ariake Sea", *Journal of Oceanography*, 74(6), pp.565-586. https://doi.org/10.1007/s10872-017-0454-9

Zeebe, R. E. & Wolf-Glandrow, D. (2001). "CO_2 in seawater: Equilibrium, kinetics, isotopes". *Elsevier Oceanography Series*, 65, pp.1-346.

Appendix A. Delft3D-WAQ Model Parameters

Table A1. Parameters for LTLE Model by Komori *et al*. (2021)

Description	Symbol	Value	Unit	Reference
State Variables				
Ammonium	C_{NH4}	*	gN/m^3	
Nitrate	C_{NO3}	*	gN/m^3	
Ortho-phosphate	C_{PO4}	*	gP/m^3	
Particulate organic carbon	C_{POC}	*	gC/m^3	
Particulate organic nitrogen	C_{PON}	*	gN/m^3	
Particulate organic phosphorus	C_{POP}	*	gP/m^3	
Particulate organic carbon in sediment	$C_{s,C}$	*	gC/m^2	
Particulate organic nitrogen in sediment	$C_{s,N}$	*	gN/m^2	
Particulate organic phosphorus in sediment	$C_{s,P}$	*	gP/m^2	
Dissolved oxygen concentration	C_{DO}	*	gO_2/m^3	
Algae biomass	C_{ALG}	*	gC/m^3	
Fluxes				
Net algae growth	B_{gro}, D_{gro}	*	$gM/m^3/day$	
Gross primary production	B_{gpp}	*	$gM/m^3/day$	
Algae respiration	B_{rsp}	*	$gM/m^3/day$	
Algae mortality	B_{mor}	*	$gM/m^3/day$	
Decomposition of POM	B_{dec}, D_{dec}	*	$gM/m^3/day$	
Settling flux	B_{set}	*	$gM/m^3/day$	
Autolysis of algae mortality	B_{aut}	*	$gM/m^3/day$	
Melting flux	B_{mel}	*	$gM/m^2/day$	
Nitrification	B_{nit}, D_{nit}	*	$gM/m^3/day$	
Reaeration	D_{rea}	*	$gO_2/m^3/day$	
Sediment oxygen demand	D_{sod}	*	$gO_2/m^3/day$	
Limiting factors				
Nutrient limitation factor for algae growth	μ_{nut}	*	-	
Radiation limitation factor for algae growth	μ_{lt}	*	-	
Nutrient limitation factor for dec. of POM	$f_{\mathrm{dec,nut}}$	*	-	
Oxygen limitation factor for nitrification	f_{ox}	*	-	

Table A1. (Continued)

Description	Symbol	Value	Unit	Reference
Parameters and constants				
Algae				
Potential maximum production rate at 20°C	α_1	1.5	day^{-1}	(D)
Potential maximum respiration rate at 20°C	α_2	0.041	day^{-1}	(Y)
Potential maximum mortality rate at 20°C	α_3	0.2	day^{-1}	(Y)
Temperature factor for primary production	β_1	1.06	-	(Y)
Temperature factor for respiration	β_2	1.07	-	(Y)
Temperature factor for mortality	β_3	1.07	-	(Y)
Half saturation constant for nitrogen for algae growth	$K_{s,N}$	0.005	gN/m^3	(G)
Half saturation constant for phosphorus for algae growth	$K_{s,P}$	0.001	gP/m^3	(G)
Light intensity at water surface	I_0	***	W/m^2	
Optimum light intensity for algae	I_{opt}	96.898	W/m^2	(Y)
Attenuation coefficient	k_{lt}	1.5	m^{-1}	(C)
Particulate organic matter				
Fraction of autolysis	α_{aut}	0.3	-	(B)
Maximum mineralization rate at 20°C of POC	$k_{\mathrm{decH},C}$	0.24	day^{-1}	(C)
Minimum mineralization rate at 20°C of POC	$k_{\mathrm{decL},C}$	0.22	day^{-1}	(C)
Maximum mineralization rate at 20°C of PON	$k_{\mathrm{decH},N}$	0.24	day^{-1}	(C)
Minimum mineralization rate at 20°C of PON	$k_{\mathrm{decL},N}$	0.08	day^{-1}	(B)
Maximum mineralization rate at 20°C of POP	$k_{\mathrm{decH},P}$	0.24	day^{-1}	(C)
Minimum mineralization rate at 20°C of POP	$k_{\mathrm{decL},P}$	0.08	day^{-1}	(B)
Temperature factor for decomposition	β_4	1.047	-	(G)
Upper limit stoichiometric constant PON	$f_{\mathrm{sU},N}$	0.15	gN/gC	(D)
Lower limit stoichiometric constant PON	$f_{\mathrm{sL},N}$	0.1	gN/gC	(D)
Upper limit stoichiometric constant POP	$f_{\mathrm{sU},P}$	0.015	gP/gC	(D)
Lower limit stoichiometric constant POP	$f_{\mathrm{sL},P}$	0.01	gP/gC	(D)
Settling velocity of POM	w_s	0.432	m/day	(Y)
Critical shear stress for POM	τ_c	0.3	N/m^2	(D)

Table A1. (Continued)

Description	Symbol	Value	Unit	Reference
Nutrients				
Fraction of ammonium in nitrogen uptake	f_{uptN}	*	-	
Critical ammonium concentration	$C_{c,NH4}$	0.01	gN/m^3	(D)
N:C ratio in algae biomass	s_N	0.16	gN/gC	(D)
P:C ratio in algae biomass	s_P	0.02	gP/gC	(D)
Potential maximum elution rate at 20°C	α_5	0.03	day^{-1}	(D)
Temperature factor for elution	β_5	1.09	-	(D)
Potential maximum nitrification rate at 20°C	α_6	0.02	day^{-1}	(Y)
Temperature factor for nitrification	β_6	1.03	-	(Y)
Dissolved oxygen				
Critical concentration of DO for nitrification	$C_{\mathrm{cr},DO}$	1	gO_2/m^3	(D)
Optimal concentration of DO for nitrification	$C_{\mathrm{op},DO}$	5	gO_2/m^3	(D)
O:C ratio in POC	s_O	2.67	gO_2/gC	(D)
O:N ratio in NO_3	s_{NO}	4.571	gO_2/gN	(D)
Reaeration factor	k_a	0.7	day^{-1}	(Y)
Saturation dissolved oxygen concentration	C_{DOs}	*	gO_2/m^3	
Chloride concentration	Cl	*	gCl/m^3	
Specified SOD	D_{sod0}	1.5	$gO_2/m^2/day$	(C)
Potential maximum SOD rate at 20°C	α_7	0.5	$gO_2/m^3/day$	(C)
Temperature factor for SOD	β_7	1.07	-	(C)
Critical concentration of DO for SOD	$C_{\mathrm{cr,sod}}$	0	gO_2/m^3	(D)
Optimum concentration of DO for SOD	$C_{\mathrm{op,sod}}$	0.5	gO_2/m^3	(C)
Physical input data				
Salinity	S	**	ppt	
Water temperature	T	**	°C	
Water depth	D	**	m	
Shear stress	τ	**	N/m^2	
*: Calculated in Delft3D-WAQ **: Calculated in Delft3D-FLOW ***: Observation data		(B): Blauw *et al.*, 2009 (C): Calibrated (D): Delft3D-WAQ (G): Gurel *et al.*, 2005 (Y): Yamaguchi *et al.*, 2018		

Table A1. (Continued)

Parameters	Value	Reference Unless otherwise noted, data are from Tadokoro and Yano (2019)
NCRatGreen	0.16	
PCRatGreen	0.02	
NH4KRIT	0.01	
TcNit	1.03	
COXNIT	1	
RcNit	0.1	Delft3D-WAQ
OOXNIT	5	
SWRear	1	
KLRear	0.7	
TCRear	1	
RcDetCS1	0.06	Corrected based on Smits (1980)
TcBMDetC	1.09	
CTMin	3	
SOD	0	Delft3D-WAQ
fSOD	0	Delft3D-WAQ
RcSOD	0.1	
TcSOD	1.07	
COXSOD	0	
OOXSOD	0.5	
PPMaxGreen	1.5	
GRespGreen	0	
Mort0Green	0.2	
MortSGreen	0.2	
SalM1Green	-999	
SalM2Green	-999	
TcDen	1.12	
RcDetNS1	0.06	Corrected based on Smits (1980)
TcBMDetN	1.09	

Table A1. (Continued)

Parameters	Value	Reference Unless otherwise noted, data are from Tadokoro and Yano (2019)
ku_dFdcC20	0.24	
kl_dFdcC20	0.22	
ku_dFdcN20	0.24	
kl_dFdcN20	0.08	
ku_dFdcP20	0.24	
kl_dFdcP20	0.08	
kT_dec	1.047	
FrAutGreen	0.3	
FrDetGreen	0.7	
RcDenSed	0.1	
CTDEN	2	
RcDetPS1	0.06	Corrected based on Smits (1980)
TcBMDetP	1.09	
SWRearCO2	0	Corrected
KLRearCO2	1	Delft3D-WAQ
VSedPOC1	0.432	
TaucSPOC1	0.3	
VSedGreen	0.1	
TaucSGreen	0.1	
KMDINgreen	0.005	
KMPgreen	0.001	
RadSatGree	96.898	
TcGroGreen	1.06	
TcDecGreen	1.07	
SWSatCO2	2	Corrected

Table A2. Parameters added or modified form the previous study in this study

Description	Symbol	Value	Unit	Reference
State variables				
Macrophytes submerged 01	C_{MAC}	*	gC/m^2	
Flux				
Macrophytes submerged 01 production	$B_{MAC,gpp}$	*	[$gC/m^2/d$]	
Limitation factor				
Water temperature limitation factor for SM01	f_{temp}	*	[-]	
Nutrient limitation factor for SM01	f_{nut}	*	[-]	
Radiation limitation factor for SM01	f_{rad}	*	[-]	
Parameters and constants				
Potential growth rate macrophytes submerged 01		3.5	[/d]	
Critical temperature for growth SM01		0	[oC]	Delft3D-WAQ
Temperature coefficient for SM01		1.06	[-]	Delft3D-WAQ
N:C ratio SM01		0.2	[-]	Delft3D-WAQ
P:C ratio SM01		0.02	[-]	Delft3D-WAQ
Half-saturation value N SM01		0.005	[gN/m^3]	Delft3D-WAQ
Half-saturation value P SM01		0.001	[gP/m^3]	Delft3D-WAQ

Table A2. (Continued)

Light intensity at the top of SM01 in Layer N		*	[W/m^2]	
Total radiation growth saturation for SM01		96.898	[W/m^2]	Komori *et al.* (2021)
Maintenance respiration Greens		5	[/d]	Modified
Threshold biomass SM01 in		0	[gC/m^2]	Delft3D-WAQ
Macrophyte distr. Function SM01		1	[-]	Delft3D-WAQ
Max Height SM 01		1.5	[m]	
Potential biomass for SM01		300	[gC/m^2]	
Habitat suitability index for SM 01		File imported	[-]	
Partial atmospheric CO2 pressure		0.000421 for 2022 0.000425 for 2023	[atm]	Observed data at St. Ryori

*: Calculated in Delft3D-WAQ

Appendix B. Observed and Simulated Values

Table B1. Observed and simulated pCO_2 (μatm)

Year	Time	Observed	Simulated-Old	Simulated-New
2022	18:00	333.63	437.73	402.29
	21:00	377.80	430.19	406.43
	0:00	394.65	422.29	409.06
	3:00	383.57	422.39	392.17
	6:00	375.47	421.35	383.76
	9:00	404.74	413.53	388.80
	12:00	392.33	398.86	398.54
	15:00	331.64	395.62	391.30
	18:00	352.96	398.34	380.71
2023	16:00	304.14	328.99	319.11
	18:00	300.21	332.32	315.91
	21:00	327.94	328.18	316.54
	0:00	321.52	322.31	316.75
	4:00	375.64	319.47	301.56
	7:00	361.91	318.80	296.34
	10:00	329.92	317.30	305.90
	13:00	306.74	331.64	328.18
	16:00	346.40	337.94	320.74
	19:00	316.63	338.59	310.48

Table B2. Observed and simulated salinity and water temperature (ºC)

		Observed		Simulated_Old		Simulated_New	
Year	Time	Salinity	Water temperature	Salinity	Water temperature	Salinity	Water temperature
2022	18:00	31.32	23.5	31.35	27.2	31.35	27.2
	21:00	29.31	22.8	31.40	26.9	31.40	26.9
	0:00	31.09	22.5	31.44	26.6	31.44	26.6
	3:00	29.37	21.4	31.34	26.2	31.34	26.2
	6:00	30.41	21.2	31.31	25.9	31.31	25.9
	9:00	30.14	21.8	31.39	25.7	31.39	25.7
	12:00	30.42	22.4	31.49	25.4	31.49	25.4
	15:00	27.1	21.9	31.47	25.1	31.47	25.1
	18:00	30.82	21.4	31.41	24.9	31.41	24.9
2023	16:00	31.24	21.2	30.22	23.8	30.22	23.8
	18:00	30.77	21.7	30.14	23.9	30.14	23.9
	21:00	28.6	20.5	30.16	23.7	30.16	23.7
	0:00	30.36	19.5	30.24	23.4	30.24	23.4
	4:00	30.96	19.3	30.11	22.8	30.11	22.8
	7:00	31.11	18.7	30.09	22.6	30.09	22.6
	10:00	31.15	20.6	30.14	23.0	30.14	23.0
	13:00	31.23	21.6	30.23	24.4	30.23	24.4
	16:00	28.97	22.1	30.13	24.6	30.13	24.6
	19:00	29.69	21.8	29.99	24.5	29.99	24.5

Table B3. Observed and simulated TA (μmol/kg) and DIC (μmol/kg)

		Observed		Simulated-Old		Simulated-New	
Year	Time	TA	DIC	TA	DIC	TA	DIC
2022	18:00	2142.3	1871.3	2047.9	1816.2	2059.6	1810.8
	21:00	2116.3	1887.2	2061.8	1826.4	2073.3	1825.7
	0:00	2144.9	1912.8	2070.4	1832.6	2081.8	1836.3
	3:00	2136.5	1916.3	2052.9	1821.2	2064.4	1817.6
	6:00	2128.2	1902.3	2046.0	1817.1	2057.6	1810.2
	9:00	2116.8	1902.6	2061.3	1827.9	2072.8	1826.4
	12:00	2135.9	1908.0	2076.6	1835.4	2087.9	1844.7
	15:00	2108.9	1874.8	2066.1	1827.4	2077.7	1835.1
	18:00	2129.0	1888.6	2051.3	1818.0	2063.3	1819.9
2023	16:00	2116.0	1850.0	2001.3	1756.3	2007.4	1756.0
	18:00	2114.7	1845.1	1984.1	1743.4	1990.0	1739.4
	21:00	2088.0	1858.2	2001.6	1756.7	2007.6	1755.4
	0:00	2119.2	1879.6	2021.8	1772.1	2028.1	1774.2
	4:00	2131.7	1916.0	1990.1	1749.4	1996.0	1744.1
	7:00	2130.7	1912.2	1979.4	1741.9	1985.1	1733.8
	10:00	2120.5	1873.6	2003.8	1758.1	2010.2	1756.9
	13:00	2145.0	1872.4	2022.2	1770.7	2028.9	1774.3
	16:00	2054.3	1826.7	1980.4	1738.7	1986.7	1734.7
	19:00	2078.2	1829.5	1947.7	1713.5	1953.5	1703.3